Glycine receptor α3K governs mobility and conductance of L/K splice variant heteropentamers

Running title: Glycine receptor α3L/K heteropentamerization

Veerle Lemmens[1,2,*], Bart Thevelein[1,*], Svenja Kankowski[3,4], Hideaki Mizuno[5],

Jochen C. Meier[4], Susana Rocha[2], Bert Brône[6], Jelle Hendrix[1,2,#]

[1] Dynamic Bioimaging Lab, Advanced Optical Microscopy Centre and Biomedical Research Institute, UHasselt, B-3590 Diepenbeek, Belgium.

[2] Molecular Imaging and Photonics, Chemistry Department, KU Leuven, B-3001 Heverlee, Belgium.

[3] Institute of Neuroanatomy and Cell Biology, Hannover Medical School, D-30625 Hannover, Germany

[4] Division Cell Physiology, Zoological Institute, Technical University Braunschweig, D-38106 Braunschweig, Germany.

[5] Laboratory of Biomolecular Network Dynamics, Biochemistry, Molecular and Structural Biology Division, Department of Chemistry, KU Leuven, B-3001 Heverlee, Belgium

[6] Neurophysiology Lab, Biomedical Research Institute, UHasselt, B-3590 Diepenbeek, Belgium.

* These authors contributed equally.

[#] Correspondence:

Jelle.hendrix@uhasselt.be

Hasselt University

Agoralaan C (BIOMED)

B-3590 Diepenbeek

Tel. +32 11 269213

Summary

The glycine receptor α3 is key to the central nervous system's physiology and involved in chronic pain and epilepsy. In this paper, Lemmens et al. reveal and functionally characterize α3 splice variant heteropentamerization via advanced single-molecule fluorescence image analysis.

Abstract

Glycine receptors (GlyRs) are ligand-gated pentameric chloride channels in the central nervous system. GlyR-α3 is a possible target for chronic pain treatment and temporal lobe epilepsy. Alternative splicing into K or L variants determines the subcellular fate and function of GlyR-α3, yet it remains to be shown whether its different splice variants can functionally co-assemble, and what the properties of such heteropentamers would be. Here, we subjected GlyR-α3 to a combined fluorescence microscopy and electrophysiology analysis. We employ masked Pearson's and dual-color spatiotemporal correlation analysis to prove that GlyR-α3 splice variants heteropentamerize, adopting the mobility of the K variant. Fluorescence-based single-subunit counting experiments revealed a variable and concentration ratio dependent hetero-stoichiometry. Via single-channel on-cell patch clamp we show heteropentameric conductances resemble those of the α3K splice variant. Our data are compatible with a model where α3 heteropentamerization fine-tunes mobility and activity of GlyR α3 channels, which is important to understand and tackle α3 related diseases.

Keywords

Glycine receptors, ligand gated ion channels, image correlation spectroscopy, single-molecule fluorescence, Pearson's correlation coefficient, subunit counting, protein co-assembly, diffusion, stoichiometry, electrophysiology, patch clamp.

Declarations

Funding

Conflicts of interest / competing interests

No conflicts of interest apply.

Ethics approval

Not applicable

Availability of data and material

All data and material are available upon request.

Code availability

Fluctuation imaging and co-localization analyses were performed in the software package PAM [71]. The software is available as source code, requiring MATLAB to run, or as pre-compiled standalone distributions for Windows or MacOS at http://www.cup.uni-muenchen.de/pc/lamb/software/pam.html or hosted in Git repositories under http://www.gitlab.com/PAM-PIE/PAM and http://www.gitlab.com/PAM-PIE/PAMcompiled. A detailed user manual is available at http://pam.readthedocs.io.

Author contributions

Conceptualization Meier J.C., Brône B. and Hendrix J.; Investigation and formal analysis Lemmens V. and Thevelein B.; Software development Hendrix J.; Writing the original draft Lemmens V., Thevelein B and Hendrix, J.; Review and editing by all authors.

3

80 **Introduction**

81 Neuronal communication in the central nervous system (CNS) is fine-tuned via ionotropic channel

82 proteins such as glycine receptors (GlyRs). Belonging to the family of pentameric ligand-gated ion

83 channels (pLGICs), GlyRs help regulate motor coordination and sensory signal processing [1, 2]. In

84 humans, GlyRs are expressed as one of three α isoforms (α1-3) that heteropentamerize with the β

85 isoform if the latter is present. In this paper we focus on the α3 isoform of GlyR, which in the human

86 body is found in the spinal cord's dorsal horn, the brain stem and the hippocampus[3] . In addition,

87 high RNA levels were also found in the cerebral cortex, the amygdala and in the pituitary gland [4]. It

88 is involved in temporal lobe epilepsy (TLE) [5-8] and, due to its crucial involvement in inflammatory

89 pain perception, it is a major target for chronic pain treatment [9]. Because of its specific localization

90 in the CNS, targeting α3 could lead to reduced side effects compared to other GlyR-α isoforms.

91 GlyR-α3 is produced as one of two possible splice variants, α3K or α3L. Post-transcriptional exclusion

92 of exon 8 from the GlyR-α3 coding mRNA [3, 10-12] results in the α3K variant lacking 15 amino acids

93 (TEAFALEKFYRFSDT) in the large intracellular loop between transmembrane α-helices TM3 and TM4

94 (Fig. 1A). GlyR-α3L is the predominant variant in a healthy brain, outweighing α3K approximately five-

95 fold. Although both variants are always co-expressed in neurons, GlyR-α3K primarily localizes

96 somatodendritically [5, 6, 13, 14], while α3L mostly localizes at the presynapse due to interaction with

97 vesicular trafficking factor SEC8 [6], where it stimulates neurotransmitter release [6, 15-17], similar to

98 other presynaptic chloride channels. Finally, neuronal cells additionally co-expressing GlyR-β

99 endogenously will also contain postsynaptic heteropentameric α-β GlyRs, due to interaction with the

100 postsynaptic scaffold protein gephyrin [18, 19].

101 Previous reports have used fluorescence microscopy and electrophysiology to investigate the

102 properties of homomeric GlyR-α3. Apart from their overall subcellular localization, fluorescence

103 fluctuation imaging and single-particle tracking revealed that in live cells both (immunostained HA-

104 tagged) splice variants exhibited free and confined diffusion in the membrane. Both fast (diffusion

105 constant D ~0.1 μm^2/s) and slow-diffusing (D ~0.01 μm^2/s) species could be observed for both variants,

106 with slow and confined diffusion being more prevalent for α3L than α3K [20, 21]. Fluorescence imaging

107 using primary spinal cord or hippocampal neurons, or HEK293 cell lines, also evidenced that α3L is

108 more prone to clustering in the cell membrane [5, 22, 23]. This suggests a role for the insert in the

109 intracellular loop in directly promoting pentamer-pentamer interactions, whether or not combined

110 with linking to immobile submembranous components that enhance the clustering process. It has also

111 been shown using cell culture based whole-cell patch clamp experiments that, overall, α3L expressing

112 cells exhibit slower desensitization kinetics than α3K [3, 24]. The longer TM3-TM4 intracellular loop

113 seems to confer a larger stability to the α3L variant leading to slower desensitization, an effect that

114 clustering seems to undo [25]. Finally, main-state single-channel conductances of 63-105 pS were

4

115   observed for the α3L variant by different groups [25-29]. For the α3K variant, one group reported a

116   similar conductance of 69 pS, suggesting the TM3-TM4 loop does not contribute to regulating the ion

117   flux through the open channel [25].

118   Besides the molecular and functional differences of the α3 homomers described above, it is intriguing

119   to know whether the two α3 splice variants can also form heteropentamers, and if they do, which

120   effects this would have on GlyR function. Indeed, the pathological effect of the increased K-to-L

121   expression ratio in TLE patients with a severe disease course hints to a functional direct interaction

122   between the splice variants [5]. The existence of α3L/K heteropentamers in HEK293 cells was already

123   suggested [22] via co-localization analysis of the differently labeled splice variants, although in this

124   report the distinction between clusters of overlapping homopentamers or actual heteropentamers

125   could not be made.

126   In this paper, we hypothesize that GlyR-α3 K/L splice variants functionally interact in a cell-biological

127   context. If so, we would like to know what the molecular and functional properties of such

128   heteropentamers are. We first develop strategies for expressing and imaging single GlyR-α3 pentamers

129   in the membrane of live cells. We then use a combination of different quantitative fluorescence

130   microscopy imaging and analysis methods including Pearson's co-localization, raster/temporal image

131   correlation spectroscopy [30, 31] and subunit counting via stepwise photobleaching [32, 33] to

132   investigate the mobility, heteropentamerization and heterostoichiometry of co-expressed GlyR-α3 K/L

133   splice variants. Then, we subject GlyR-α3 expressing cells to functional analysis via single-channel patch

134   clamp. In the discussion section we integrate the results from the different types of experiments we

135   performed and compare this with the present state of knowledge to better understand the cell-

136   biological consequences of GlyR splice variant heteropentamerization.

137

138 **Results**

139 Advanced methodology for imaging single-pentamer properties of glycine receptors

140 Physiologically, GlyR-α3 molecules are present both as single pentamers and clusters of pentamers. As

141 we were specifically interested in single pentamers, we first developed a cell-based fluorescent GlyR

142 expression system and an analysis methodology that allows specifically analyzing the molecular

143 properties of single GlyR-α3 pentamers in a way that is unbiased by clusters. First, to visualize the α3L

144 and α3K isoforms of GlyR, we used plasmids encoding the GlyR N-terminally tagged with a green (eGFP)

145 or red (mCherry) fluorescent protein (FP) (Fig. 1A, Fig. S1E-G) and transiently transfected these in

146 HEK293 cells. These do not express GlyR endogenously but are known to be a relevant model system

147 for studying GlyRs [3]. Immunocytochemistry (Fig. S1) and whole-cell patch-clamp electrophysiology

148 (Fig. S2) confirmed a subcellular distribution and activity much like the endogenous situation,

149 respectively, of the FP-tagged receptor.

150
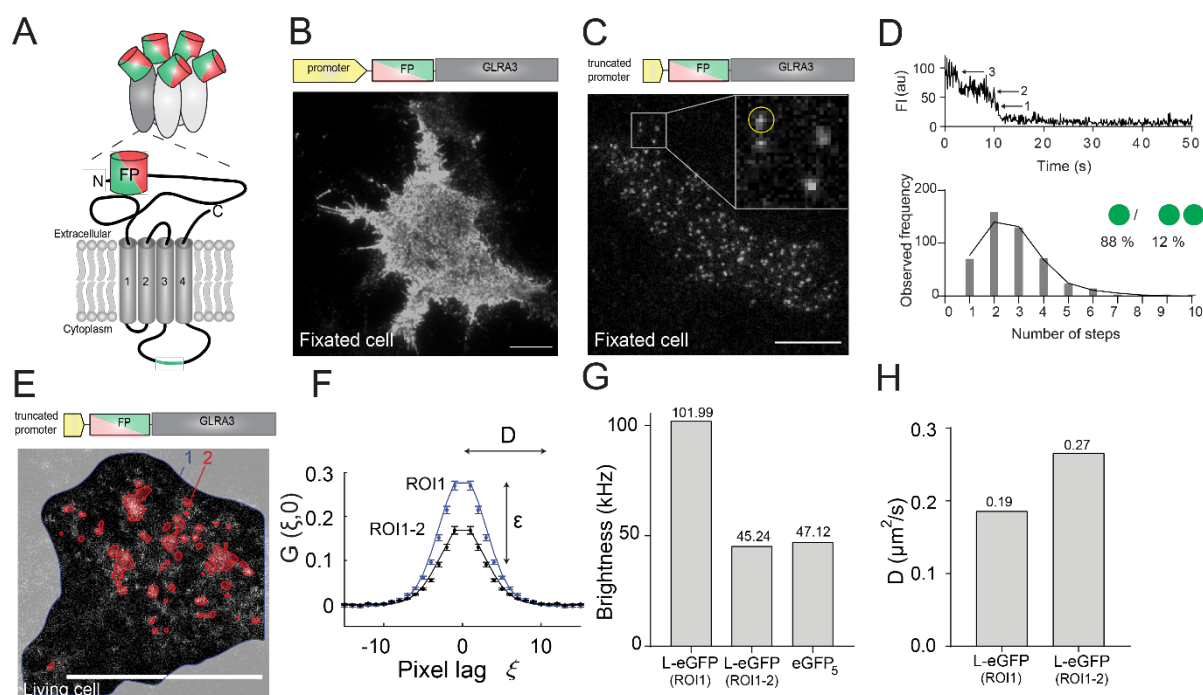
151

152 **Fig. 1: Low copy number imaging of GlyR-**α3L-FP in HEK293 cells allows quantifying single

153 pentamer properties. A) Subunit structure of GlyR-α3-FP with the fluorescent protein eGFP or

154 mCherry (FP) fused to the terminus of the extracellular N-terminal domain and the position of

155 the TM3-TM4 loop insert for GlyR-α3L in green. B) Representative cell with high copy number

156 GlyR expression from a plasmid with a stong promoter. Scale bar, 10 µm. C) Representative

157 fixated cell with low copy number GlyR expression using a plasmid with a truncated promoter.

158 Scale bar, 10 µm. The inset is a magnification of the area indicated by the white square, white

159 spots indicate single receptors, the yellow circle corresponds to the data in the upper part of

6

160   panel D. D) Step-wise photobleaching subunit counting identify low numbers of fluorescent

161   eGFP per fluorescent spot in the low copy number cells. E) Confocal fluorescence image of a live

162   cell expressing GlyR used for RICS analysis. The edge of the cell is outlined in blue (region of

163   interest, ROI1) and the high intensity clusters, automatically selected via frame-to-frame

164   intensity thresholding (see Materials and Methods for more details), are highlighted in red

165   (ROI2). Scale bar, 10 μm. F) The 1D section of the average 2D RICS autocorrelation function (the

166   reader is referred to Fig. S3A-B for images of the 2D correlation functions) at spatial lag (ξ, 0) of

167   a confocal image series of GlyR-α3L-eGFP expressing cells using either all pixels within ROI1 or

168   within ROI1 minus ROI2. The reader is also referred to Video S1-2 for the different ROIs. The

169   mean brightness ε and mean diffusion coefficient are determined from the amplitude and shape

170   of the correlation function, respectively. G) Representative example of the molecular brightness

171   (in kphotons/second) of diffusing GlyR-α3L-eGFP assemblies within ROI1 or within ROI1 minus

172   ROI2, and, as a reference, molecular brightness of diffusing cytosolic $eGFP_5$ measured as close

173   to the bottom membrane as possible. H) Representative example of the diffusion coefficient of

174   diffusing GlyR-α3L-eGFP within ROI1 or within ROI1 minus ROI2.

175

176   Then, we followed a three-pronged approach to achieve the required low (single-molecule) and

177   intermediate (10-100 nM) expression levels that are ideally suited for the planned single-pentamer

178   analyses and for the diffusion analysis, respectively. We truncated the CMV promotor (similar to [34]),

179   reduced the amount of GlyR encoding plasmid DNA while retaining the transfection efficiency via

180   co-transfection with a non-coding plasmid [35] and limited the time between transfection and fixation

181   or live-cell imaging. Using total internal reflection fluorescence microscopy (TIRFM) we imaged fixated

182   cells expressing the normal- or low-expressing GlyR-α3L-eGFP plasmids (Fig. 1B-C). Indeed, with the

183   latter plasmids we could easily find cells that clearly exhibited individual diffraction limited fluorescent

184   spots (Fig. 1C), presumably single pentamers.

185   We next set out to prove whether these spots corresponded to single GlyR pentamers by recording

186   time-lapse fluorescence images of transiently transfected cells and counting the number of eGFP

187   molecules per diffraction-limited spot using single-spot photobleaching step measurements (Fig. 1D,

188   top). As can be seen from the frequency distribution of the number of steps, a variety of bleaching

189   steps ranging from 1 to 10 was observed (Fig. 1D, bottom). This has been observed before in bleaching

190   experiments of GlyR-α1 in HEK293 cells [32, 36] and is attributed to a mixture of incomplete maturation

191   of the fluorescent proteins, prebleaching of the eGFP, and single pentamers that are overlapping at a

192   spatial scale smaller than the optical resolution. To analyze the data quantitatively, we fitted the

193   distribution to a binomial model (Eq. 1, see Materials and Methods). This analysis resulted in a

194   probability of 47% for eGFP to be maturated and unbleached and in 88% of spots not overlapping with

7

195   other spots. Both of these values are similar to previous experiments on GlyR-α1 in HEK293 cells [32,

196   36]. This experiment thus suggests that in the low-expressing HEK293 cells, about 88% of detected

197   fluorescent spots were likely single pentamers.

198   Finally, to corroborate that the majority of GlyRs detected in the cell membrane were indeed single

199   pentamers, we used confocal raster image correlation spectroscopy (RICS). Practically, we performed

200   experiments in cells with intermediate expression levels of GlyR-α3L-eGFP (ideally 10-100 nM [37])

201   (Fig. 1E). In such cells, we observed both regions with diffuse fluorescence, as well as regions with high-

202   intensity fluorescent clusters, the latter presumably being GlyR aggregates that have been observed

203   before [20]. After spatial autocorrelation of the images (Eq. 5) and fitting the resulting data to Eq. 6,

204   we obtained both the molecular brightness ε (Eq. 7) and the mobility (diffusion constant, D) of the GlyR

205   complexes diffusing in the membrane (Fig. 1F). The ε informs on the average number of fluorescing

206   eGFP moieties in the diffusing complexes and, via comparison with a control protein, can be used to

207   assess their average stoichiometry. The D, on the other hand, reports on the average size of these

208   diffusing complexes, with slower diffusion indicative of larger complexes. When we included all pixels

209   belonging to the cell membrane into the analysis (ROI1 in Fig. 1E, Fig. S3A and Video S1), the ε that we

210   measured was significantly higher than that of a control protein, a cytosolic tandem eGFP pentamer

211   (eGFP5) that we measured as close to the cell membrane as possible (Fig. 1G). When we additionally

212   excluded the regions with an intense fluorescence signal (ROI1 minus ROI2 in Fig. 1E, Fig. S3B and Video

213   S2), the brightness ε of the diffusing GlyR complexes was indistinguishable from that of the eGFP5

214   control Fig. 1G. Additionally, this experiment seems to show that properties of single GlyR pentamers

215   can be specifically studied, in the case of intermediate-expression cells, by masking out regions

216   containing clusters. The observed diffusion constant also depended on the ROI that was selected for

217   the RICS analysis. Indeed, diffusion analysis in 'ROI1 minus ROI2' resulted in overall increased mobility,

218   which directly proves the masking procedure efficiently removed the high-stoichiometry GlyR clusters

219   (Fig. 1H).

220   In summary, we generated HEK293 cells expressing low amounts of GlyR-α3 splice variants labeled

221   with fluorescent proteins and validated single-molecule and fluctuation imaging tools that allow

222   focusing on the properties of single pentameric complexes excluding GlyR clusters. In the rest of the

223   paper all analyses are performed on single GlyR pentamers, unless explicitly stated otherwise.

224   Specifically, we take a closer look at the two splice variants, and at what happens when they are co-

225   expressed in cells.

226

227 <u>Single homopentameric K and L variants exhibit a different diffusion signature</u>

228 As a follow-up of the work of Notelaers et al. [20, 21], we next investigated the mobility of the two

229 different splice variants GlyR-α3L-eGFP and GlyR-α3K-eGFP with RICS [38, 39] and temporal image

230 correlation spectroscopy (TICS) [40], using image masking to specifically focus on single pentamers.

231 RICS, which analyses µs-ms intensity fluctuations occurring within confocal image frames, is typically

232 used to quantify the mobility of faster protein populations ($D \approx$ 0.1-500 µm^2/s) while TICS, in which

233 tens-of-milliseconds camera pixel intensity fluctuation are correlated over time, is typically used to

234 quantify the mobility of proteins diffusing on a relatively slow timescale ($D \approx$ 0.001-0.1 µm^2/s). Parallel

235 application of both techniques allow identifying and characterizing different possible mobile protein

236 populations [41]. Essential to this is choosing imaging conditions suited to the type of diffusion process

237 (for RICS, see [42], for TICS, see [43]).

238 For RICS, we acquired confocal image series of living cells expressing either GlyR-α3L-eGFP or GlyR-

239 α3K-eGFP at 37 °C as illustrated in Fig. 2A. Because in confocal microscopy the laser scans pixel per

240 pixel and line per line while proteins diffuse, the resulting image will contain spatial fluorescence

241 intensity fluctuations along any direction in the image, as depicted in Fig. 2B along the direction of a

242 single line scan. We spatially correlated each image frame in the series (Eq. 5) and via fitting of the

243 average spatial autocorrelation function (Fig. 2C-D, Eq. 6), we determined that the diffusion

244 coefficients D of GlyR-α3L-eGFP (D = 0.26±0.11 µm^2/s) and GlyR-α3K-eGFP (D = 0.29±0.08 µm^2/s) were

245 within experimental error the same (Fig. 2E). At least within the timescale of a single RICS image frame,

246 the K and L variants thus exhibit similar diffusion.
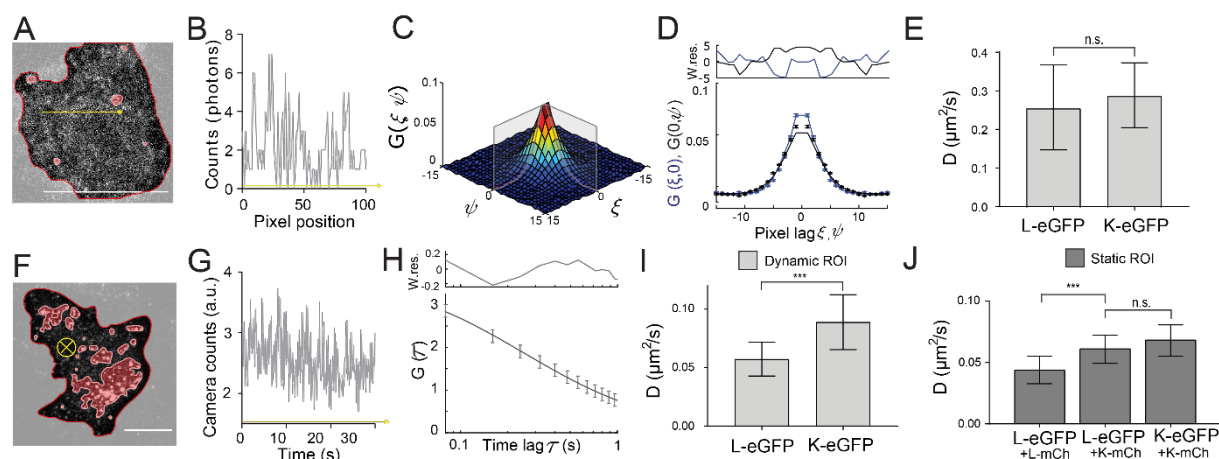
247

248 **Fig. 2: RICS and TICS evidence two diffusive subpopulations of single GlyR pentamers.** A)

249 Representative confocal microscopy image of the first frame from an image series of a HEK293

250 cell expressing GlyR-α3L-eGFP. Frame-based intensity thresholding was used to remove GlyR

251 clusters and the extracellular region from the analysis. Scale bar 10 µm. B) Photon count values

252 fluctuating along the yellow arrow in A. C) 3D autocorrelation with the grey outlining showing

253 the average (ξ, 0) and (0,φ) autocorrelation function. D) Average (ξ, 0) and (0,φ) autocorrelation

9

254   function and fit. Top graph displays the weighted residuals for the fit in the bottom graph. E)

255   Average diffusion coefficient and standard deviation obtained via RICS for GlyR-α3L-eGFP and

256   GlyR-α3K-eGFP. F) Representative TIRF microscopy image of the first frame from an image series

257   of a HEK293 cell expressing GlyR-α3L-eGFP. Frame-based intensity thresholding was applied to

258   remove GlyR clusters (indicated in red) and the extracellular region (indicated in light gray). Scale

259   bar 10 μm. G) Camera count values fluctuating along the yellow arrow in F which is directed into

260   the plane of the image to represent its direction through time. H) Average temporal

261   autocorrelation function and fit. Top graph displays the weighted residuals for the fit in the

262   bottom graph. I) The average diffusion coefficient and standard deviation obtained via TICS for

263   single GlyR-α3L-eGFP and GlyR-α3K-eGFP. Here, a dynamic mask was used, calculated per frame,

264   to omit both mobile and immobile GlyR clusters from the analysis. J) The average diffusion

265   coefficient and standard deviation obtained via TICS for GlyR-α3L-eGFP when co-expressed with

266   GlyR-α3K-mCh or GlyR-α3L-mCh compared to co-expression of GlyR-α3K-eGFP with GlyR-α3K-

267   mCh. Image masking was based on the average intensity of the time series, so only static clusters

268   were removed. Error bars on the bar graphs represent the standard deviation from n = 9-22

269   different cell measurements (Table S1-2). *** p-value < 0.001 obtained via an unpaired two

270   sample t-test with unequal variance of the data.

271

272   For TICS, time-lapse images were acquired using TIRF-based widefield microscopy in living cells at room

273   temperature (Fig. 2F). As the frame rate using a camera is much faster than for confocal microscopy,

274   and oftentimes similar to the time it takes molecules to diffuse in and out of image pixels, fluorescence

275   intensities tend to fluctuate from frame to frame due to molecular diffusion, as illustrated in Fig. 2G.

276   By temporally autocorrelating each pixel's fluorescence time trace (Eq. 10) and fitting a model to the

277   obtained mean temporal autocorrelation function (Fig. 2H, Eq. 11), the diffusion coefficient can

278   likewise be determined. In this way we obtained a diffusion coefficient of D = 0.089±0.023 μm^2/s for

279   GlyR-α3K-eGFP and a significantly lower diffusion coefficient of D = 0.057±0.014 μm^2/s for GlyR-α3L-

280   eGFP (Fig. 1I). First, this analysis reveals a second diffusive GlyR species, as values for D were

281   significantly lower as observed with RICS, even when RICS measurement were performed at RT (Fig.

282   S2F). More interestingly, however, the slower component of the L variant is significantly lower than

283   the slow component of the K variant. To investigate the possibility that this could be related to

284   inefficient removal of clusters from the analysis, which would affect the clustering-prone L variant

285   more than the K variant, and thus also the observed mobility (Fig. S3C) [5, 22, 23], we performed a

286   detailed comparison of different masking procedures (Fig. S3D). This showed a dependence of the

287   observed D for both K and L on the type of mask used: whole cell (Video S3), static mask (Video S4,

288   mask calculated on the average of all frames), dynamic mask (Video S5, calculated per frame), a

10

289   significantly slower diffusion of the L variant was always observed. In other words, when looking at

290   diffusing of single pentamers of GlyR-α3 on the slow TICS timescale, the L variant exhibits a slower

291   mobility than the K variant.

292   Finally, we wanted to investigate whether co-expression of K would affect the mobility of L at the level

293   of pentamers. Practically, we co-expressed GlyR-α3L-eGFP and the red mCherry FP-tagged version of

294   the short GlyR isoform (GlyR-α3K-mCh) and performed single-color TICS on the acquired eGFP channel

295   image series. Interestingly, we observed an increased diffusion coefficient for GlyR-α3L-eGFP in the

296   presence of GlyR-α3K-mCh (Fig. 2J, Table S2, D = 0.061±0.01 µm2/s; the value is slightly different than

297   in Fig. 2I because of the different mask used) as compared to cells co-expressing GlyR-α3L-eGFP and

298   GlyR-α3L-mCh (Fig. 2J, Table S2, D = 0.044±0.01 µm2/s) or as compared to GlyR-α3L-eGFP alone

299   (Fig. S3D, Table S2, D = 0.047±0.01 µm2/s). As expected, co-expression of GlyR-α3K-eGFP and GlyR-

300   α3K-mCh (Table S2, D = 0.068±0.01 µm2/s) did not affect the mobility of the former as compared to

301   GlyR-α3K-eGFP alone (Table S2, D = 0.074±0.01 µm2/s). These results are strongly indicative of a direct

302   K-L interaction at the level of single pentamers, which we will investigate using dual-color imaging.

303

304   <u>Co-localization and co-diffusion proves GlyR-α3L/K heteropentamerization</u>

305   To investigate whether GlyR heteropentamerization could be the cause of the increased mobility

306   observed for GlyR-α3L-eGFP when co-expressed with GlyR-α3K-mCherry in the membrane of HEK293

307   cells, we recorded dual-color images via alternating-excitation TIRF microscopy (Fig. 3A).

308
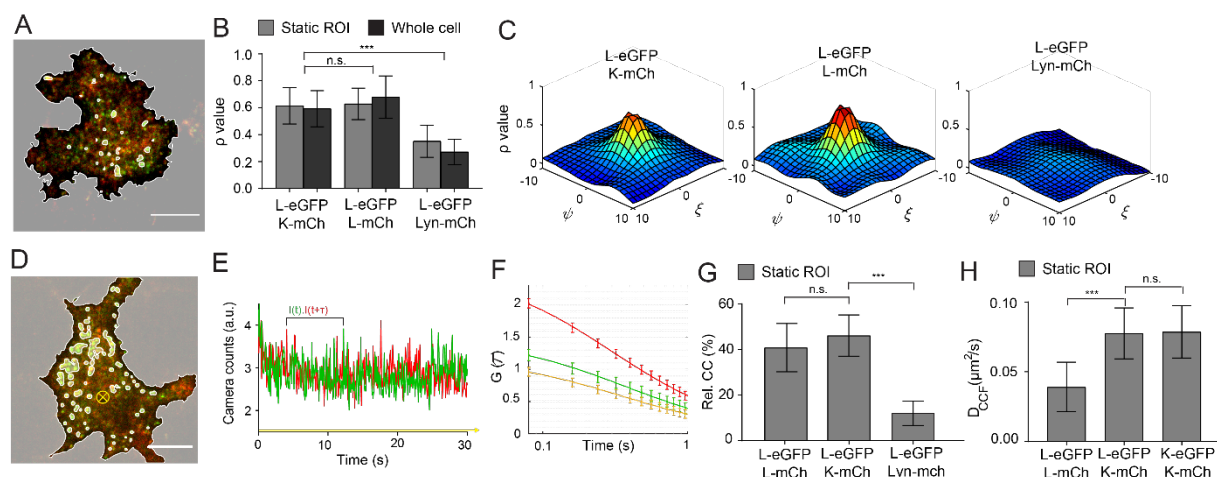
309

310   **Fig. 3: Co-localization and co-diffusion of GlyR-α3 isoforms in HEK293 cells at single-molecule**

311   **expression confirms the presence of GlyR-α3L/K heteropentamers.** A) Representative dual-

312   color TIRF image of a HEK293 cell co-expressing GlyR-α3L-eGFP (green) and GlyR-α3K-mCherry

313   (red). Using intensity thresholding over the average of the 5 first frames the cell membrane was

314   selected and bright regions containing GlyR clusters were omitted. Scale bar 10 µm. B) Pearson's

11

315   correlation coefficient of cells expressing GlyR-α3L-eGFP and GlyR-α3K-mCherry and cells co-

316   expressing GlyR-α3L-eGFP and GlyR-α3L-mCherry plasmids. Both experimental groups have

317   significantly higher co-localization compared to the negative control with GlyR-α3L-eGFP and

318   Lyn-mCherry. The ρ values are shown for cells including (grey) and excluding (dark grey) GlyR

319   clusters. C) Spatial ρ from representative cells expressing GlyR-α3L-eGFP and GlyR-α3K-mCherry

320   (left), GlyR-α3L-eGFP and GlyR-α3L-mCherry (middle) or GlyR-α3L-eGFP and Lyn-mCherry

321   (right). D) Representative dual-color TIRF image of a HEK293 cell co-expressing GlyR-α3L-eGFP

322   (green) and GlyR-α3K-mCherry (red). Intensity thresholding was applied over the average of the

323   400 frames (static ROI) to remove GlyR clusters and the extracellular region. Scale bar 10 μm. E)

324   Dual-color fluorescence trace for one selected pixel over time (yellow arrow orthogonal to the

325   image in D). F) Mean temporal autocorrelation (green and red) and cross-correlation (yellow) of

326   all included pixels after intensity thresholding. Error bars are the 95% confidence intervals. G)

327   The relative cross-correlation (Eq. 12) for cells expressing GlyR-α3L-eGFP and GlyR-α3K-

328   mCherry, GlyR-α3L-eGFP and GlyR-α3L-mCherry plasmids, and the negative control with GlyR-

329   α3L-eGFP and Lyn-mCherry. H) Average diffusion coefficient and standard deviation obtained

330   via TICCS for cells co-expressing GlyR-α3L-eGFP and GlyR-α3K-mCh or GlyR-α3L-mCh, or for cells

331   co-expressing GlyR-α3K-eGFP and GlyR-α3K-mCh. Error bars represent the standard deviation

332   from $n = 5\text{-}22$ measurements (see Table S2-3 for n). *** p-value < 0.001 obtained via an

333   unpaired two sample t-test with unequal variance of the data.

334

335 To quantify the similarity of the two images and hence the colocalization of the two splice variants in

336 the membrane, we calculated the Pearson's correlation coefficient ρ (Eq. 8). The ρ describes the

337 degree of correlation between green and red channel pixel intensities of a dual-color image [44, 45].

338 The values of ρ can range from 1 to -1, with 1 a perfect correlation, 0 when there is no correlation and

339 -1 for when there is an inverse relationship (exclusion) between the images. The pixels included in the

340 analysis were confined to the region of the cell membrane since the extracellular region holds pixels

341 with both low green and red intensity values which falsely increases the ρ value [46]. In addition, when

342 cells contained regions with clustering GlyRs, these regions were also omitted by static ROI intensity

343 thresholding to ensure Pearson's analysis was performed only on the heteropentamer fraction. This

344 revealed a positive Pearson's correlation coefficient calculated for images of cells co-expressing GlyR-

345 α3L and GlyR-α3K, similar to the one calculated for cells co-expressing GlyR-α3L labeled with eGFP and

346 mCherry (Fig. 3B), and significantly higher than for the negative control cells co-expressing GlyR-α3L-

347 eGFP and the monomeric membrane protein Lyn-mCherry that does not interact with GlyR. To confirm

348 that the Pearson's coefficient was indeed determined mainly by the fluorescent receptors, and less by

349 cellular background, ρ was calculated as a function of the pixel shift between the images in the x and

12

350   *y* direction (Fig. 3C). For cells expressing GlyR-α3L and GlyR-α3K a clear positive peak was seen,

351   indicative of real co-localization. For cells expressing non-interacting GlyR-α3L-eGFP and Lyn-mCherry,

352   this peak was generally absent or very small and wide (Fig. 3C, right), indicative of a specific co-

353   localization.

354   Although Pearson's correlation is an excellent qualitative proof for protein-protein co-localization, to

355   more directly investigate the hetero-oligomerization of the slowly diffusing GlyR-α3 population we

356   used dual-color cross-correlation TICS (TICCS) in HEK293 cells co-expressing GlyR-α3L-eGFP and

357   GlyR-α3K-mCherry [31, 40]. For TICCS, image acquisition of the bottom membrane was performed

358   using dual-color fast alternating TIRF-based excitation microscopy (Fig. 3D). For each pixel position in

359   the image series, the fluorescence time traces (Fig. 3E) were temporally auto- and cross-correlated

360   (Fig. 3F, Eq. 10). While the temporal autocorrelation and cross-correlation functions on their own allow

361   determining molecular parameters such as mobility (Eq. 11), the relative cross-correlation additionally

362   is a proof for their co-diffusion, and even a measure for the interaction affinity between them [47]. For

363   cells co-expressing GlyR-α3L-eGFP and GlyR-α3K-mCherry we measured a high relative

364   cross-correlation (Fig. 3G, Eq. 12) that was similar to cells co-expressing GlyR-α3L-eGFP and

365   GlyR-α3L-mCherry. This is a result from a similar high interaction affinity. Note that even for constantly

366   interacting or even covalently linked molecules the maximum interaction value is typically around 50-

367   60% (it never reaches the theoretical 100%) since it is limited due to factors such as incomplete

368   fluorescent protein maturation or the partial overlap between green and red microscope detection

369   volumes [48]. As a negative control, we analyzed cells containing GlyR-α3L-eGFP and Lyn-mCherry

370   (Fig. 3G). We observed a very low cross-correlation amplitude (Fig. S3E) and significantly lower relative

371   cross-correlation.

372   In contrast to single-color fluctuation experiments, dual-color TICCS offers the additional possibility to

373   focus specifically on the diffusion properties of the heteropentameric complexes containing both eGFP

374   and mCherry fluorophores. In line with the single-color experiments, these data also show that GlyR-

375   α3L/K complexes exhibit higher diffusion coefficients compared to GlyR-α3L-eGFP/mCherry

376   homopentamers (Fig. 3H, Table S2). Interestingly though, the heteropentamer *D* derived from the

377   cross-correlation function was completely indistinguishable from that of K homopentamers, indicating

378   that the K splice variant dominates the diffusion pattern of K/L heteropentamers. Together, the

379   Pearson's correlation and dual color TICCS experiments prove that GlyR-α3L and GlyR-α3K are

380   localizing and diffusing as a complex. As the masked analyses we perform allow focusing on GlyR

381   pentamers, this must mean the GlyR-α3K and GlyR-α3L splice variants can heteropentamerize.

382   Moreover, heteropentamer diffusion is dictated by the short-loop splice variant K. We next wondered

383   whether these heteropentamers existed in a defined heterostoichiometry or not.

384

385 The stoichiometry of GlyR heteropentamers depends on the relative subtype expression

386 To provide further insights into the stoichiometry of heteropentamers we performed two types of

387 experiments: single-molecule step-wise photobleaching and molecular brightness analysis. For the first

388 experiment, we performed continuous TIRFM single-molecule imaging of the eGFP labels in fixated

389 cells co-expressing GlyR-α3L-eGFP and GlyR-α3K-mCherry and analyzed the resulting single-molecule

390 traces with a step-finding algorithm to count the number of fluorescing eGFPs in a single complex

391 (Fig. 4A). As the co-localization and fluctuation experiments showed that under such experimental

392 conditions, these complexes are most likely heteropentamers containing both eGFP and mCherry

393 fluorophores, it is expected that compared to samples containing GlyR-α3L-eGFP homopentamers

394 (Fig. 1D), the number of eGFP moieties per complex should be lower. Indeed, the experimental data

395 revealed a distribution with, on average, less eGFP subunits per spot compared to GlyR-α3L-eGFP

396 homopentamers (Fig. 4B; Kolmogorov-Smirnov test p < 0.01).

397
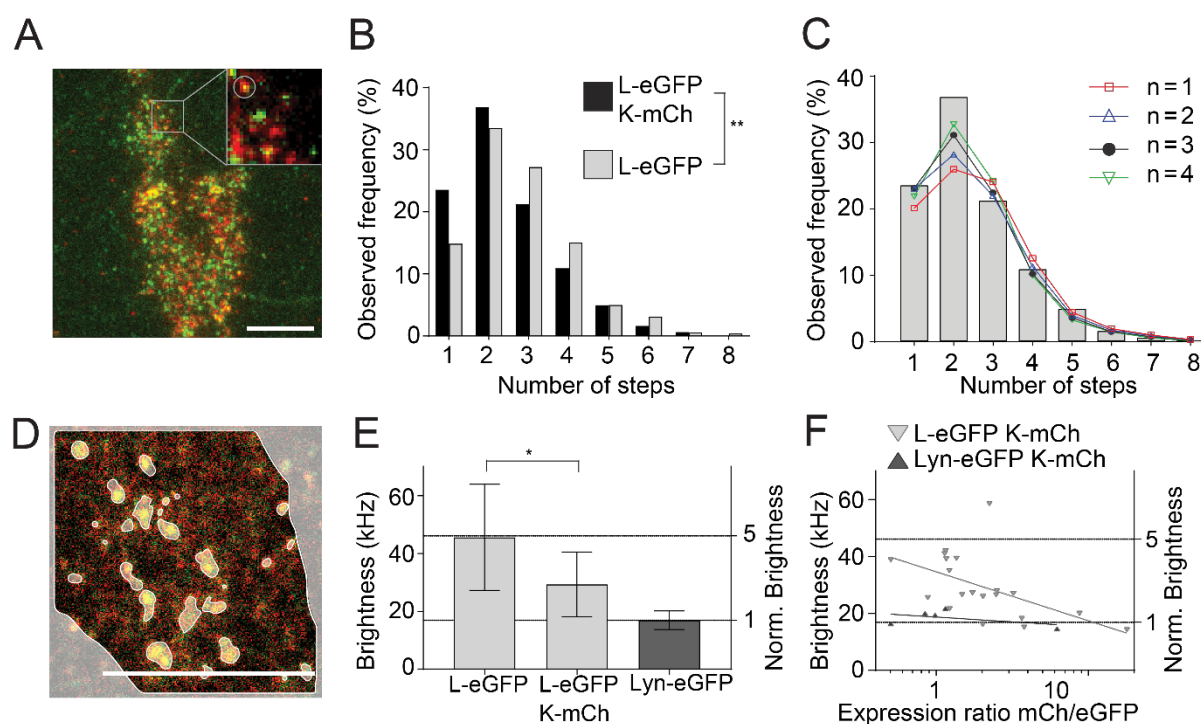
398
399

400 Fig. 4: Automated subunit analysis and molecular brightness analysis shows the effect of relative

401 expression on the GlyR stoichiometry. A) Representative images of HEK293 cells expressing

402 GlyR-α3L-eGFP (green) and GlyR-α3K-mCherry (red). Scale bar 10 μm. B) Step distribution

403 histogram of GlyR-α3L-eGFP in the presence (light grey, 301 spots) and absence (black, 477

404 spots) of GlyR-α3K-mCherry. In the presence of GlyR-α3K-mCherry there is a significant shift

405 towards a lower number of GlyR-α3L-eGFP subunits. **p-value < 0.01 obtained with

406 Kolmogorov-Smirnov test. C) Fitted binomial distribution functions with a sum of a 5th order

14

407   binomial and n^{th} order (n=1-4) binomial. See Table S4 for heteromeric fraction and p-value for

408   the fit ($\chi 2$-test). D) Representative confocal microscopy image of the first frame from an image

409   series of a HEK293 cell expressing GlyR-α3L-eGFP and GlyR-α3K-mCherry. Scale bar 10 μm. E)

410   Molecular brightness comparison of the membrane-bound monomeric protein Lyn-eGFP to

411   GlyR-α3L-eGFP in either the presence or absence of GlyR-α3K-mCherry. Error bars represent the

412   standard deviation from n = 5-20 measurements (see Table S5 for n). * p-value < 0.05 obtained

413   via an unpaired two sample t-test with unequal variance of the data. F) Molecular brightness of

414   GlyR-α3L-eGFP (light grey) and monomeric Lyn-eGFP (dark grey) in the presence of variable

415   amount of GlyR-α3K-mCherry. The semilog line fit shows a decrease in brightness for GlyR-α3L-

416   eGFP upon increasing ratio of GlyR-α3K-mCherry to GlyR-α3L-eGFP.

417

418   We fitted the resulting step frequency distribution using two binomials, one representing the

419   heteropentamer (up to 4 GlyR-α3L-eGFP subunits) and the other the homopentamer fraction (Eq. 2,

420   Fig. 4C). The maturation probability (pm) and probability of overlapping spots (1-A) was fixed to 47%

421   and 12%, respectively, based on the experiments on homopentamers (Fig. 1D), while the relative

422   fraction of heteropentamers was fitted. The goodness-of-fit obtained via the $\chi 2$-test (Supplementary

423   Table S4) was best for a 3rd order binomial and a heteropentameric fraction of 36% (goodness-of-fit

424   P-value from a χ2 test = 0.725, with 1 being a perfect fit). However, as relatively good fits were obtained

425   as well with a 2nd (P-value = 0.332) or 4th (p-value = 0.672) order binomial for a heteropentameric

426   fraction of 23% and 67% respectively, these analyses are compatible with a scenario where

427   heteropentamers contain on average 2-4 eGFP-containing subunits.

428   For the molecular brightness analysis, we recorded a confocal image series of living cells expressing

429   GlyR-α3L-eGFP alone, or together with GlyR-α3K-mCherry (Fig. 4D) and analyzed the molecular

430   brightness in the eGFP detection channel via dynamic-ROI based RICS (Eq. 7). As expected, this

431   revealed a significantly lower molecular brightness for L/K heteropentamers as compared to L

432   homopentamers (Fig. 4E, Table S5). Interestingly, the molecular brightness calculated in the eGFP

433   channel scaled with the signal (count rate) ratio of GlyR-α3K-mCh compared to GlyR-α3L-eGFP (Fig.

434   4F), and a few cells even exhibited a similar molecular brightness as observed for the monomeric

435   control Lyn-eGFP, meaning the presence of heteropentameric GlyRs with only a single L-eGFP subunit.

436   Taken together, these experiments suggest the stoichiometry of GlyR-α3 heteropentamers is not fixed

437   but variable, and depends on the relative expression of the L and K subtypes.

438

439   <u>The α3K electrophysiological signature dominates in heteropentamers</u>

440   At this stage, we revealed the existence of K/L heteropentamers and investigated their molecular

441   organisation. Lastly, we wanted to investigate possible functional differences between

442 heteropentamers and homopentamers. Indeed, this might help to understand the consequences of an

443 aberrant L/K ratio as observed in TLE. Practically, we used on-cell single-channel patch-clamp

444 electrophysiology as opposed to whole-cell measurements to avoid averaging out activities of different

445 co-existing species. Moreover, to verify the GlyR expression levels and ensure patch clamp

446 measurements were performed under identical conditions as the fluorescence experiments, the patch

447 clamp setup was mounted directly onto the single-molecules fluorescence microscope used for the

448 stepwise photobleaching and TICS/TICCS experiments. Cells were transfected with either GlyR-α3L-

449 eGFP or GlyR-α3K-mCherry, or with both. Importantly, the transfection conditions were similar to

450 those used in the TICCS measurements, where we showed a high prevalence of heteropentamers for

451 cells transfected with both plasmids. We selected cells with proper expression levels using

452 fluorescence microscopy (Fig. 5A) and then performed on-cell single-channel electrophysiology to

453 determine different possible conductance states (Fig. 5B).
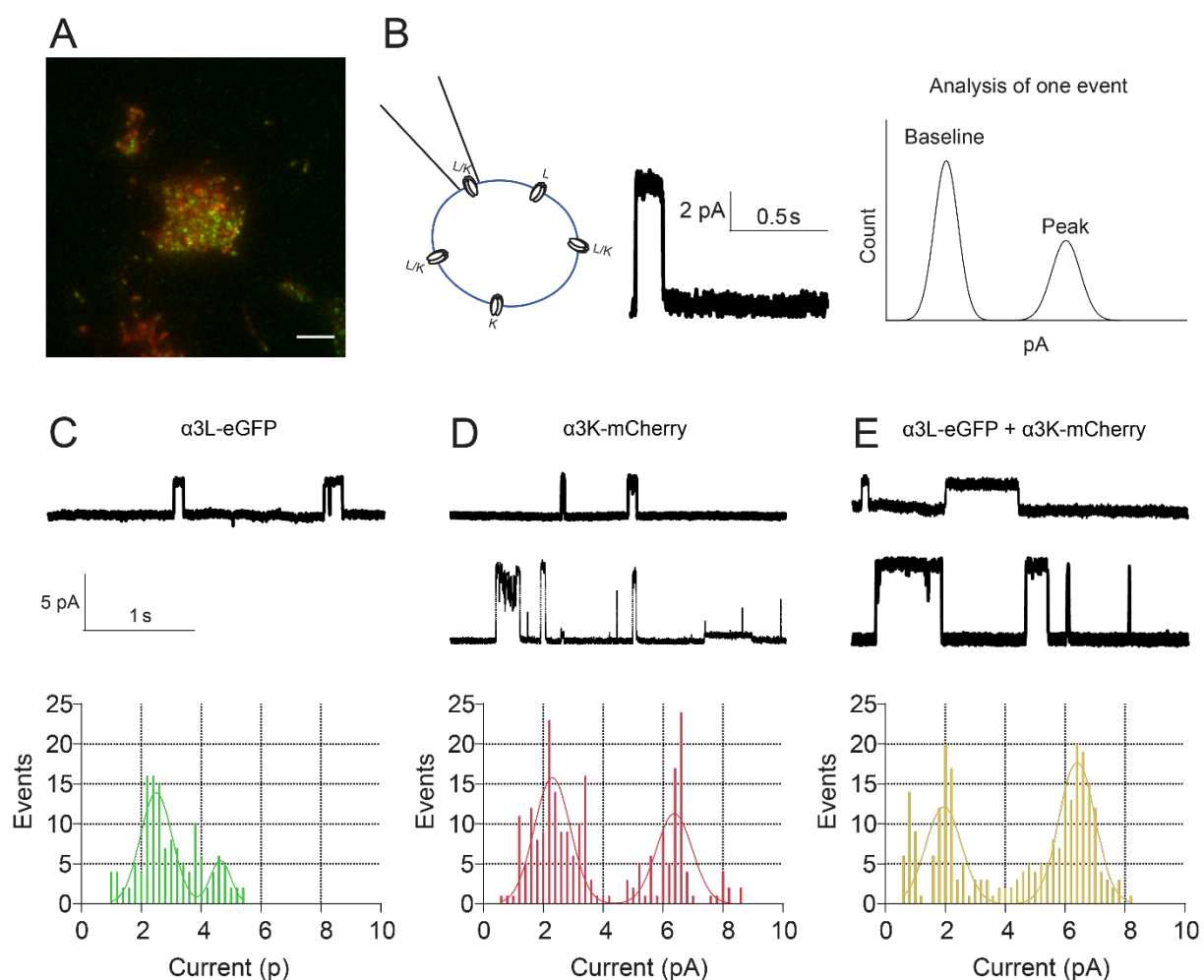
454

455 **Fig. 5.** On-cell measurements show activated α**3K yields a high-current conducting state.** A)

456 Transfected cells are identified by eGFP or mCherry fluorescence. Scale bar 5 μm. B) Example of

457 a current time trace and analysis of a single opening event during which a peak current is seen.

458 On-cell measurements are performed by placing a patch pipette to measure chloride currents

459   through a single glycine receptor. For each single channel event, a histogram of all measured

460   currents is fit with a double gaussian, yielding a best fit value for the mean baseline current and

461   the mean peak current. Subtracting the mean baseline current from the mean peak current

462   yields the 'mean current of the single opening event' C-E) Examples of single-channel current

463   traces with accompanying histograms of 'mean currents of the single opening events' of cells

464   transfected with α3L (n = 10, red), α3K (n = 18, blue) or α3L and α3K (n = 15, black). Histograms

465   were fit with a double Gaussian to identify the most common peak amplitudes of single events.

466   For α3K and for α3L and α3K an example of both a low and a high current single-channel trace

467   is shown.

468

469   Like this, we could reveal two frequently occurring states for all tested conditions (Fig. 5C-E), with the

470   first conductance state (around 2.3 pA) similar for all conditions (K, L and K/L), but the second

471   conductance state showing significantly lower currents for α3L (around 4.7 pA) compared to α3K and

472   α3L + α3K (around 6.4 pA). Contrary to what is known from [25-29] literature, our data seem to

473   indicate that the presence of the α3K subunit in the GlyR yields higher currents.

Discussion

The glycine receptor is a ligand-gated chloride channel that plays a crucial role in the general physiology of the CNS. Its α3 isoform, in particular, is involved epilepsy and chronic pain [5, 9, 26]. Two splice variants of α3 exist (Fig. 1A). As homopentamers, the splice variants differ in subneuronal distribution, electrical conductance and desensitization, clustering tendency, interactions with subcellular components and diffusion properties [3, 5, 6, 20-22], yet it is not known whether L and K variants can heteropentamerize. Indeed, such a process may lead to new or intermediate properties, or properties biased more towards one variant or the other. In an attempt to provide a more detailed fundamental cell-biological understanding of the working of GlyR-α3, we thus investigated the hypothesis that the different splice variants of GlyR-α3 can assemble into functional heteropentamers. To prove this hypothesis via advanced fluorescence imaging we first had to set up a new quantitative image analysis methodology for studying single pentamers in a complex sample, cell membranes containing both single pentamers and clusters of the same protein. Then, using this methodology we revisited prior work on the diffusion properties of GlyR-α3 splice variants in HEK293 cells to unequivocally prove whether RNA splicing determines the membrane mobility of the protein. Only hereafter could we embark on proving the existence of GlyR-α3L/K heteropentamers, and on quantifying their molecular and functional properties.

Tools for studying defined molecular species in the case of oligomerization/clustering

A first methodological aim was to set up the necessary experimental tools to quantify single GlyR-α3 pentamer properties in cells. This is particularly challenging because of the tendency of GlyR-α3 to form subcellular clusters [5, 22, 23] that would overshadow the analysis. In previous research done by Notelaers et al., GlyR-α3 properties were investigated using fluctuation spectroscopy, single-molecule and super-resolution fluorescence methods, yet it was not explicitly investigated which observed species were representative of single pentamers or clusters [20-22]. Indeed, although image correlation spectroscopy (ICS) methods are quite robust in quantifying concentrations, diffusion and stoichiometry for monodisperse samples [49], they perform particularly badly in the case of polydisperse ones containing clusters, aggregates or multimeric species [50-52]. Here, we exploited the molecular fluorescence brightness of fluorescent protein labeled GlyR splice variants to validate that our methodology does specifically allow studying single pentamer properties. On the one hand, we performed subunit counting via stepwise photobleaching [32, 33] experiments in low-expressing cells in which fluorescent homomeric GlyR-α3L-eGFP was present as clearly discernable fluorescent spots (Fig. 1C-D). This way we found that the number of fluorescence bleaching steps per spot was similar to the previously studied GlyR-α1 under non-clustering conditions in HEK293 cells [32, 36]. On the other hand, we used a more recent extension of classical ICS called arbitrary-region ICS (ARICS)

18

509   [50], where image series are segmented based on the local pixel fluorescence intensity, to specifically

510   quantify the average molecular fluorescence brightness for single GlyR pentamer complexes diffusing

511   in the live cell membrane (Fig. 1E-H; Video S1-2). With this analysis, we could show that results for (the

512   more clustering-prone) homomeric GlyR-α3L-eGFP expressing cells were in line with non-clustering

513   stoichiometric control proteins. This finally proved that our cellular expression system, HEK293 cells

514   expressing fluorescent protein labeled GlyR splice variants from a crippled CMV promotor, and single-

515   molecule photobleaching and segmented ICS analyses, are adequate for studying single pentamer

516   properties, even when a non-negligible clustering subpopulation is present. Apart from the

517   investigations performed in the rest of our paper, the methodological toolbox presented here can be

518   applied for examining protein interactions, oligomerization, mobility and stoichiometry of other

519   oligomeric receptors or multimeric proteins. Also, relative to the original methodological publication

520   on segmented ICS [50] (detailed protocol in [53]), we did extend our in-house developed software for

521   robust segmented single- and dual-color raster and temporal ICS analysis. This software can be

522   downloaded   free-of-charge   (see   Materials   and   Methods),   is   fully   documented

523   (https://pam.readthedocs.io/en/latest/mia.html), can be operated via a convenient graphical user

524   interface from Microsoft and Apple operating systems, accepts a variety of images/videos, and can

525   export figures and videos directly in publication-format.

526

527   <u>Specific subcellular interactions of single GlyR-α3L pentamers decrease their membrane mobility</u>

528   Physiologically, GlyR-α3 is present in cells both as clustered and single pentamers. While α3K is more

529   randomly distributed over the cell membrane, the situation for α3L is balanced somewhat more in

530   favor of clusters. The α3L interacts with submembranous components specifically enriched at the

531   presynapse, where it can promote (at glutamatergic nerve termini) neurotransmitter release [6].

532   Functionally, clustering of α3L thus seems to be an efficient way to promote this local enrichment.

533   Notelaers et al. previously reported that overall, the subcellular mobility of α3L was lower than of α3K

534   [20, 21]. For systems undergoing Brownian diffusion, the mobility (more specifically, the translational

535   diffusion constant) of a freely-diffusing entity scales inversely with its size (Einstein-Smoluchovski

536   relation). For membrane proteins in particular, mobility scales with the radius of the transmembrane

537   region [54] [54, 55]. For the specific case of GlyR-α3L, receptor clustering would increase the size of

538   the diffusing complex, and this would reduce mobility. Likewise, however, strong interactions of GlyR-

539   α3 with large or immobile submembranous components would also likely reduce its overall mobility.

540   As a follow-up of the work of Notelaers et al., we investigated whether a difference in single-pentamer

541   mobility between the L and K variants can also be detected using our experimental setup. To this

542   extent, we performed both confocal and TIRF-based microscopy and ICS analysis of GlyR-α3 expressing

543   HEK293 cells to study the diffusion properties of the two splice variants. We segmented the images

19

544   before ICS analysis to exclude those pixel regions containing GlyR clusters. Via confocal raster ICS (RICS)

545   analysis we observed a fast freely diffusing component for both isoforms with similar diffusion

546   coefficients ($D\alpha$3L = 0.26±0.11 μm^2/s and $D\alpha$3K = 0.29±0.08 μm^2/s) (Fig. 2A-E, Table S1). The existence

547   of this freely diffusing component, that has been described before [21], suggests that at least a fraction

548   of the GlyR-α3 population does not interact with immobile cellular components, or that the mere

549   limited affinity for the latter defines the presence of a significant unbound component. The presence

550   of functional GlyRs with relatively high mobility is, however, not surprising. It could allow for a faster

551   reconstitution of non-desensitized GlyR receptor pools, as has been shown previously for the AMPA

552   receptor, another ligand-gated ion channel [56]. When we studied the diffusion of single GlyR-α3

553   pentamers using TIRF-based temporal ICS (TICS), we observed a second, much less mobile species for

554   both splice variants, which, interestingly, was even less mobile for α3L as compared to α3K ($D\alpha$3L =

555   0.057±0.014 μm^2/s and $D\alpha$3K = 0.089±0.023 μm^2/s) (Fig. 2F-I, Table S1-S2). This observation, in term,

556   strongly suggests that the 15-residue-longer loop of GlyR-α3L relative to GlyR-α3K does indeed

557   stabilize interactions with cellular interaction partners such as proteins or lipids, independent of GlyR

558   clustering [6]. For primary neuron hippocampal cells, vesicular transport protein SEC8 targets the GlyR-

559   α3L to the presynapse, and in vivo, GlyR-α3L was indeed detected at presynaptic terminals of

560   glutamatergic and GABAergic neurons [6]. An interesting follow-up study would be to use site-directed

561   mutagenesis of the insert region to more closely study sequence motifs of GlyR-α3L binding partners

562   that control axonal receptor trafficking and localization. Conversely, GlyR-α3K is mainly distributed

563   somatodendritically, but is also expected to be present in axonal and presynaptic compartments as

564   this splice variant lacks a subcellular targeting signal and hence diffuses throughout the neuronal

565   plasma membrane. This notion is furthermore supported by a recent study showing that there is no

566   GlyR-β protein expression in hippocampal neurons [57], which could target the GlyR-α/β

567   heteropentamers to postsynaptic gephyrin-positive scaffolds [19, 58].

568

569   <u>GlyR-α3L and GlyR-α3K splice variants form heteropentamers of variable stoichiometry.</u>

570   Co-clusters of GlyR-α3 splice variants have already been reported [22]. The single-color TICS

571   experiments we performed in the present study, however, provided a first hint towards a direct

572   interaction between α3L and α3K splice variants in the form of heteropentamers, since co-expression

573   of α3K increased the mobility of single α3L pentamers ($D_{\alpha3L}$ = 0.047 ± 0.012 μm^2/s and $D_{\alpha3L+K}$ = 0.061

574   ± 0.011 μm^2/s) (Table S2). Hetero-oligomers of different isoforms of GlyR-α/β [59] and of other ion

575   channels such as the NMDA receptors have been described before, and also the biogenesis of GlyR-α3

576   would be compatible with it [60]. For GlyR-α3 they are of specific interest because of the differential

577   subcellular localization of splice variants [6] and because of their different electrophysiological

578   desensitization signatures [3].

579 To provide a more conclusive answer, we first demonstrated co-localization between GlyR-α3L and

580 GlyR-α3K upon co-expression in HEK293 cells using a spatial version of Pearson's colocalization analysis

581 that is more robust against coincidental pixel co-localization (Fig. 3A-C, Fig. S3H, Table S3) [44, 61].

582 Subsequently, we used dual color temporal ICS (TICCS) to unequivocally demonstrate, for the first time,

583 heteropentamerization of GlyR-α3L and GlyR-α3K (Fig. 3D-G, Table S2). Finally, we employed direct

584 subunit counting via stepwise photobleaching to quantify that the average stoichiometry of

585 heteropentamers is 2-4 α3L-eGFP-containing subunits (Fig. 4A-C, Table S4). A non-negligible

586 homomeric fraction was also present in all datasets, which furthermore supports the absence of a

587 defined heterostoichiometry. Direct subunit counting via stepwise photobleaching was previously

588 used to show that α1 and β isoforms, genetically labeled with fluorescent proteins, heteropentamerize

589 in a $\alpha3\beta_2$ stoichiometry [59]. Finally, we carried out molecular brightness analysis to reveal that the

590 heterostoichiometry is indeed variable and depends on the expression ratio of both splice variants (Fig.

591 4D-F, Table S5). Putting all stoichiometry data together we did not provide any evidence for a highly

592 specific α3L/K stoichiometry.

593

594 <u>GlyR-α3L/K heteropentamers have GlyR-α3K-like mobility and conductance characteristics.</u>

595 The presence of heteropentamers can have several implications for GlyR-α3 function. In this paper, we

596 investigated the subcellular mobility and electrophysiological signature of heteropentamers. Single-

597 color TICS provides a readout of mobility, and evidenced that co-expression of α3K increased the

598 mobility of α3L (Fig. 2J, Table S2). Of course, in the case of a subcellular mixture of homo- and

599 heteropentamers, such single-color measurements only provide an average view, which is why we next

600 performed a mobility analysis of only those species containing both α3K and α3L via image cross-

601 correlation analysis via dual-color temporal ICS (TICCS) (Fig. 3H, Table S2). From these experiments it

602 became apparent that the diffusion signature of the K isoform is dominant for the mobility of the

603 heteropentamers. This additionally suggests that the subcellular interactions of α3L that render its

604 mobility slow are multivalent rather than monovalent. As many as 5 units of α3L thus seem to be

605 needed to result in its homomeric mobility signature. This might mean that the affinity of subcellular

606 interactions of α3L is rather low, and that an avidity effect leads to the observed reduced mobility of

607 homomers. Finally, combined on-cell patch clamp and fluorescence microscopy allowed us to

608 investigate the single channel current of GlyR-α3 in cells expressing both GlyR-α3L-eGFP and GlyR-α3K-

609 mCherry. A GlyR-α3K-shifted conductance was observed for cells containing heteropentamers, which

610 was larger in amplitude compared to currents from GlyR-α3L-eGFP homopentamers.

611 As GlyR-α3L adopts the mobility signature of GlyR-α3K in heteropentamers, in regions of the brain

612 where co-expression of GlyR-α3L and GlyR-α3K occurs, this could mean that heteropentamerization

613 influences GlyR renewal in the plasma membrane, and as a result GlyR functionality. Consequently,

614 this further stresses the importance of well-regulated alternative splicing for GlyR-α3 signaling. As in

615 healthy people there is an increased presence of GlyR-α3L compared to GlyR-α3K, a small increase in

616 alternative splicing would have an effect on even more GlyR-α3L pentamers due to

617 heteropentamerization. Due to heteropentamerization a higher fraction of GlyR-α3L containing

618 pentamers will have a higher mobility, which could enable faster reconstitution of the

619 non-desensitized GlyR receptor pool [56]. The results from electrophysiology in particular also point to

620 the possibility that the neuronal output can be increased by GlyR-α3 heteropentamers, particularly in

621 conditions such as TLE where increased RNA editing and resulting gain-of-function receptors lever out

622 rules of homeostatic regulation of the neuronal output [6, 14]. Importantly, subcellular trafficking and

623 localization (pre- or postsynaptic, or e.g. in the distal and basolateral membrane compartments of

624 epithelial cells) must be logically and interpretively distinguished from terms that describe single

625 channel signatures of mobility and electrophysiology (conductance states). Indeed, a single receptor

626 pentamer with specific mobility and conductance states can lead to very different outcomes depending

627 on its subcellular localization. For example, due to its very small surface, the electrical capacity (C) of a

628 presynapse is much lower compared to the somatodendritic compartment, and hence, one single

629 channel conductance of chloride ions (Q) through the presynaptic plasma membrane will have a much

630 greater impact on membrane potential (U) compared to the same conductance in the somatodendritic

631 compartment ($\Delta U = Q/C$).

632 **<u>Conclusion</u>**

633 In this work, we investigated the long (L) and short (K) intracellular loop splice variants of the GlyR-α3

634 isoform, that is related to chronic pain and temporal lobe epilepsy. We unambiguously showed that

635 these splice variants co-assemble into electrophysiologically active heteropentamers in live HEK293

636 cells. To do this, we had to set up and validate a combination of advanced single-molecule

637 fluorescence, fluorescence fluctuation correlation and patch clamp methods, as the GlyR-α3 tends to

638 cluster inside cell membrane, and this clustering is extraordinarily challenging for quantitative

639 investigations. First and foremost, this work constitutes a methodological framework that can be used

640 for investigating other types of complex hetero-oligomerizing molecular systems in a cell-biological

641 context. Biologically, it turned out that, while the GlyR-α3L was well-known to determine the

642 subcellular localization of GlyR-α3 channels, GlyR-α3K is leading in the regulation of both the in-

643 membrane mobility of GlyR-α3, as well as in the ion channel's activity. Indeed, heteropentamers were

644 both more mobile than L homomers, and exhibited a larger open-state electrical conductance. Future

645 research could be aimed at studying GlyR heteropentamer clustering, localisation and acitivity in

646 primary neuron cells, as this would corroborate the importance of heteropentamers in neuronal

647 signaling. Likewise, measuring channel open times would prove that heteropentamerization is

648 important for fine-tuning of neuronal activity, which would, in turn, provide insights into the

649 desensitization behaviour of heteropentamers.

650

Materials and methods

DNA plasmids

651

652

653 Plasmids encoding mouse GlyR-α3L or α3K containing an N-terminal eGFP or mCherry were already

654 described [62] or obtained accordingly using standard molecular cloning technology by replacing

655 mCherry with eGFP. N-terminal eGFP insert was amplified with PCR (5'-

656 CGGTCTCCGGAATGGTGAGCAAGGGC-3' and 5'-GGCCTCCGGACTTGTACAGCTCGTCCATGC-3'), the GlyR-

657 α3L/K plasmids and the amplified eGFP insert were digested with BspE1. The vector plasmids were

658 treated with calf intestine phosphatase before the ligation was performed. The enhancer region of the

659 cytomegalovirus promotor in the GlyR-α3-coding plasmids was shortened similar as in [34] to reduce

660 expression levels by mutagenesis. We did this by amplification of the GlyR-FP plasmids using PCR with

661 primers 5'-ATATGGTACCTGGGAGGTCTATATAAGCAGAG-3' and 5'-

662 ATAAGGTACCCCAGGCGGGCCATTTACCGTA-3' followed by digestion with KpnI (ThermoFisher

663 Scientific, Merelbeke, Belgium) and ligation using instant sticky-end ligase Master mix (NEB, Bioké

664 Leiden, Nederland). Plasmids used as a negative control (Lyn-FP) were first used in [63] as a negative

665 control for membrane receptor dimerization and encode the tyrosine-protein kinase Lyn coupled to a

666 fluorescent protein eGFP or mCherry. Plasmids expressing eGFP or an oligomeric chain of 3 or 5 eGFPs

667 (eGFP, eGFP$_3$ and eGFP$_5$) previously used in [64] were used as an stoichiometric reference.

668

Cell culture and transfection

669

670 Human embryonic kidney 293 cells (HEK293 cells, provided by Dr. R. Koninckx, Jessa Hospital, Hasselt,

671 Belgium) were cultured up to a maximum passage number of 20, at 37 °C and under a humidified

672 5% CO_2 atmosphere in complete DMEM medium (D6429, Sigma-Aldrich, Overijse, Belgium)

673 supplemented with 10% FCS (Sigma-Aldrich). At least 24 h before transfection, 150,000 cells were

674 plated in complete medium in a 35-mm diameter #1.5 (170 μm glass thickness) glass bottom dish

675 (MatTek, Bratislava, Slovak Republic). Cells were transfected via calcium phosphate-DNA

676 co-precipitation [65]. The phosphate-DNA mix contained 86 μL HEPES-buffered saline (HBS) (280 mM

677 NaCl, 10 mM KCl, 15 mM D-glucose, 1.5 mM $Na_2HPO_4.2H_2O$, 50 mM HEPES, pH 7.1,) and 2000 ng total

678 plasmid DNA per dish including the 50-1000 ng FP-tagged encoding plasmids supplemented with an

679 empty plasmid vector (pCAG-FALSE, Addgene plasmid #89689) depending on the aimed fluorescence

680 level [35]. To this mix 5.1 μL 2.5 M $CaCl_2$ was added, and after 10 min of incubation at room

681 temperature (RT) the mix was added dropwise to the cells.

24

682 <u>Immunostaining</u>

683 Fixated cells expressing human GLRA3 were permeabilized at RT with permeabilization buffer (40 mL

684 PBS, 2 g sucrose, 400 μL 10% Triton X-100) during 5 min, after which the cells were washed twice with

685 washing buffer (40 mL PBS + 40 μL Triton X-100 10%). Next, cells were incubated for 10 min with

686 proteinase K (0.1%, Thermo Fisher Scientific, Merelbeke, Belgium) for antigen retrieval. After washing

687 once again with washing buffer, a blocking buffer (40 mL PBS + 0.4 g BSA + 40 μL Triton X-100 10%)

688 was added to the cells. Finally, cells were incubated for 1 h with the primary anti-GLRA2 (1/2000 in

689 blocking buffer; ab97628 Abcam, Cambridge, England), washed 3 times with blocking buffer and

690 incubated for 2 h with Alexa 647 anti-rabbit (1/250, A21247, Thermo Fisher Scientific). After washing

691 the cells 3 times with PBS, the cells were stored at 4 °C for limited time.

692

693 <u>Total internal reflection and widefield fluorescence microscopy imaging</u>

694 A Zeiss ELYRA PS.1 inverted microscope with a Plan-Apochromat 100x/1.46 oil DIC M27 objective lens

695 and Andor iXon+ 897 EMCCD camera operated at EM gain ~200 was used in total internal reflection

696 fluorescence (TIRF) mode to selectively excite molecules near (< 200 nm) the bottom cell membrane.

697 Images were recorded at room temperature using a multiband emission filter LBF 488/561 at a

698 resolution of 256×256 pixels^2 and a pixel size of 150 nm. The 488 nm and 561 nm HR diode-pumped

699 solid-state lasers were used. Immunostaining imaging was done on the same setup, using an additional

700 642 nm HR diode-pumped solid-state laser. The reported laser powers were measured on the objective

701 lens with immersion oil using a calibrated S170C microscope slide power sensor head (Thorlabs,

702 Dortmund, Germany). Imaging was done using the ZEN software (Zeiss).

703

704 <u>Subunit counting by photobleaching analysis</u>

705 TIRF images were acquired as decribed above using cells transfected with 50 ng GlyR-α3L-eGFP and 0-

706 500 ng GlyR-α3K-mCherry which were fixated 22 h post-transfection for 24 h at 4 °C using 3% (w/V)

707 paraformaldehyde in phosphate buffered saline. Before acquiring the images for the photobleachinig

708 analysis, in each cell mCherry was photobleached with the 561 nm laser (5% power, 2.5 mW) in order

709 to eliminate Förster resonance energy transfer between eGFP and mCherry. Next, 2000 frames were

710 acquired at 100 ms per frame using the 488 nm laser at high enough power to induce step-wise

711 photobleaching (1.5% power, 660 μW). Data analysis was performed using the Progressive Idealization

712 and Filtering (PIF) software kindly provided by Dr. Rikard Blunck [32]. Molecules were located by

713 selecting of 5×5 pixels^2 spots with the signal-to-noise ($\delta F/F$) setting at 20%. Next, intensity time traces

714 were extracted from a 3×3 pixels^2 region in the center of each spot. Partially overlapping spots were

715 excluded from analysis. Photobleaching steps were identified via a step-finding algorithm when steps

716 had a minimum length of 3 frames, and steps were not allowed to vary more than 60% in amplitude

25

717   compared to other steps in the time trace. In addition, a minimal step signal-to-noise value of 2 was

718   required. Cells with more than 10% accepted traces were included in the step frequency histogram.

719   The step distribution of cells expressing only GlyR-α3L-eGFP was analyzed using the sum of two

720   binomial distributions:

$$B(x; n + 2n, p_m) \qquad\qquad\qquad\qquad \text{(Eq. 1)}$$

$$= A \frac{n!}{x!\,(n-x!)} p_m{}^x (1-p_m)^{n-x} + (1$$

$$- A) \frac{2n!}{x!\,(2n-x!)} p_m{}^x (1-p_m)^{2n-x}$$

721

722   where B is the likelihood of observing x bleaching steps, n is the number of fluorescent eGFP

723   molecules present in a single GlyR complex ($n = 5$), p_m is the probality that the fluorophore is

724   maturated and non-bleached at the start of the recording, A is the fraction of spots containing not

725   more than one GlyR complex and $1-A$ is the fraction of spots containing two GlyR complexes. This

726   equation assumes the fraction of spots containing more than two pentamers is negligible. In general,

727   the p_m-value reported in studies using subunit counting via stepwise photobleaching is typically on the

728   low side (50-80%) [32, 33, 66] compared to other studies (~80%) [67, 68]. The broad range is appointed

729   to variability between experimental groups such as the used cell line, fluorescent protein [69],

730   temperature during maturation [32], cell fixation and fluorophore prebleaching [70].

731   To describe the step distribution of cells expressiong both GlyR-α3L-eGFP and GlyR-α3K-mCherry and

732   determinte the stoichiometry (*het*) of the heteropentamers, Eq. 1 was extended to:

$$B(x; n + 2n + het + 2het, p_m) \qquad\qquad\qquad\qquad \text{(Eq. 2)}$$

$$= H[B(x; n + 2n, p_m)] + (1 - H)\,[B(x; het + 2het, p_m)]$$

733

734   Here H represents the fraction of homopentamers and *1-H* represents the fraction of heteropentamers

735   in the sample. Fitting this equation to the bleaching histograms of cells transfected with both, GlyR-

736   α3L-eGFP and GlyR-α3K-mCherry, gives best fit values for H and *het*. Goodness-of-fit was determined

737   using the chi-squared test. A good fit is indicated by a low χ^2 value with $p > 0.05$, the model does not

738   fit the data if $p < 0.05$ [59].

739

740   <u>Correlation analysis</u>

741   Fluctuation imaging and co-localization analyses were performed in the software package PAM [71].

742   In all equations that follow, pre-processed intensity images $I_i(x, y, t)$ are converted into fluctuation

743   images $\delta I_i(x, y, t)$ prior to correlation analysis by subtracting the mean image intensity $\langle I_i \rangle$:

$$\delta I_i(x, y, t) = I_i(x, y, t) - \langle I_i \rangle \qquad\qquad\qquad\qquad \text{(Eq. 3)}$$

744 where i is the imaging channel, (x, y, t) denote the pixel coordinates and the angled brackets

745 represent the average of all pixels included into the region-of-interest used for analysis.

746

747 <u>Raster image correlation spectroscopy</u>

748 We used an inverted Zeiss LSM880 laser scanning microscope with a Plan-Apochromat 63x/1.4 Oil DIC

749 M27 oil objective and MBS488/594 beam splittere to image live cells transfected with 100 ng GlyR-

750 α3L-eGFP, 100 ng GlyR-α3K-eGFP or 50 ng Lyn-eGFP alone and/or combined with 0-1000 ng GlyR-α3K-

751 mCherry, between 22-28 h post-transfection. Since RICS is ideally suited for capturing fast dynamics

752 [31, 38, 41], the cells were held at 37 °C. However, to allow comparisons of RICS and TICS data, we did

753 carry out limited RICS experiments at RT too (Fig. S3F). This revealed that the species observed with

754 RICS still exhibited faster diffusion than those observed with TICS when measured at RT, and thus

755 indeed represents a different subpopulation. Images were collected using parameters appropriate for

756 RICS [42], i.e. 256×256 pixels^2 with a 50 nm pixel size. Pixel dwell, line and image times were 8.19 µs,

757 4.92 ms and 1.26 s, respectively. The eGFP species were excited with a 488 nm argon-ion laser (0.3%,

758 1 µW) and mCherry species with a 594 nm HeNe laser (1%, 6 µW). Fluorescence was detected using a

759 spectral detector (Zeiss Quasar) operated in photon counting mode in 23 spectral bins with ~9 nm bin

760 width ranging from 490 nm to 695 nm. For quantitative analysis of eGFP-tagged molecules, bins 1-11

761 (490 nm to 589 nm) were summed for further analysis. Prior to autocorrelation analysis, we excluded

762 contributions from slow processes such as cell and cell organelle movement using a moving average

763 correction according to [39, 41, 72]:

$$I_{RICS}(x, y, f) = I(x, y, f) - \langle I(x, y, f) \rangle_{\Delta F} + \langle I \rangle_{XYF} \qquad \text{(Eq. 4)}$$

764 in which $I(x, y, f)$ corresponds to each individual image, $\langle I(x, y, f) \rangle_{\Delta F}$ is the local mean image

765 calculated over a short 3-frame interval from frame $f - \Delta F$ to frame $f + \Delta F$ with $\Delta F = 1$, and $\langle I \rangle_{XYF}$

766 is the mean intensity over all frames. Next, pixels outside the cell were removed by freehand-drawing

767 based selection of the cell membrane, while GlyR clusters were removed using frame-based intensity

768 thresholding. Specifically, both green and red images were first individually masked by intensity

769 thresholding to remove (equalize to zero) pixels belonging to high-intensity clusters of fluorescence

770 [50]. The final mask contained pixels that were included in each individual image's mask and was

771 smoothed using a 3×3 median filter as described above for co-localization analysis. Subsequently, the

772 autocorrelation function was calculated per image frame using the arbitrary region-of-interest RICS

773 (ARICS) algorithm [50]:

$$G(\xi, \psi) = \frac{\langle \delta I_{RICS}(x, y) \cdot \delta I_{RICS}(x + \xi, y + \psi) \rangle}{\langle I_{RICS} \rangle^2} \qquad \text{(Eq. 5)}$$

774 in which ξ and ψ are the spatial lags in pixels, the $\cdot$ is the correlation operator, the angled brackets

775 represent the average of all included pixels within the mask and $\langle I_{RICS} \rangle$ is the average of all moving-

776 average corrected pixels included into the region-of-interest used for analysis. To compare different

777 datasets, we often plot only the (ξ, 0) correlations (example in Fig. 1F) or (ξ, 0) and (0, ψ) correlations

778 (example in Fig. 2D). Finally, the autocorrelation function was fitted with a one-component model

779 assuming a two-dimensional Gaussian point spread function to obtain the diffusion coefficient, D, and

780 average number of molecules in the focus, N.

$$G(\xi, \psi) = \frac{\gamma}{N} \left(1 + \frac{4D \left| \xi\tau_p + \psi \tau_l \right|}{\omega_r^2} \right)^{-1} exp \left(- \frac{\delta r^2 (\xi^2 + \psi^2)}{\omega_r^2 + 4D \left| \xi\tau_p + \psi \tau_l \right|} \right) \qquad \text{(Eq. 6)}$$

781 Here γ is the shape factor for a 2D Gaussian and equals $2^{-3/2}$ [73], τ_p and τ_l are pixel and line dwell

782 times, δ_r is the pixel size and ω_r the lateral waist of the focus determined by calibration

783 measurements (Fig. S4B). The RICS data was also used for calculating the molecular brightness of eGFP-

784 containing diffusing molecules. Brightness (ε), expressed in kilophotons emitted per diffusing complex

785 per second at the center of the confocal spot, was calculated by dividing the mean intensity of the

786 image series (F) by the number of molecules obtained via RICS autocorrelation analysis (N_{ACF1})

$$\varepsilon = \frac{F}{N_{ACF1}}. \qquad \text{(Eq. 7)}$$

787 As stoichiometric references, cells were transfected with 5-10 ng eGFP, eGFP$_3$ or eGFP$_5$ encoding

788 plasmids and investigated 22-28 h post-transfection as described above. When determining N, the

789 moving average correction bias on the correlation amplitude was also corrected for as described

790 before (Eq. 11 in [50]). Finally, stably focusing on the bottom membrane was achieved using a Zeiss

791 Definite Focus.2 which acquired 60 frames at two different z-positions above the coverslip with an

792 interval of 0.4 μm, alternating height each image frame, after which the time series at the z-position

793 with highest average intensity was selected for analysis. We did also observe a clear effect of focus

794 height above the coverslip on the molecular brightness, but not on the diffusion coefficient as shown

795 in Fig. S3G, and as described before [41].

796

797 <u>Pearson's co-localization analysis</u>

798 A 400-frame TIRF image series of live cells transfected with 100 ng GlyR-α3-eGFP and 150 ng GlyR-α3-

799 mCherry or 50 ng Lyn-mCherry was acquired 22h-28h post transfection at 80 ms per frame using

800 alternating 2-color excitation. The eGFP species were excited during 20 ms at 488 nm (0.75% power,

801 ~330 μW), followed by 20 ms excitation of the mCherry species at 561 nm (1.5% power, ~750 μW). A

802 modified image correlation calculation was used to calculate the Pearson's correlation coefficient ρ

803 and to check the specificity of ρ [44, 61]. Image masking was performed as for RICS analysis. The ρ of

804 the masked images was then calculated using:

$$\rho(\xi, \psi) = \frac{\langle \delta I_1 (x,y) \cdot \delta I_2 (x + \xi, y + \psi) \rangle}{\langle \sigma_1 \rangle \cdot \langle \sigma_2 \rangle} \qquad \text{(Eq. 8)}$$

805   The $\rho(0,0)$ is the classical Pearson's coefficient, $\rho \approx 1$ means green- and red-labeled containing

806   molecular complexes are overlapping, $\rho \approx 0$ means a random distribution and a value approaching -1

807   would mean exclusion. For the Pearson's analysis, the same data as for fluctuation analysis was used,

808   which contains significant shot noise. We therefore made an average of the first 5 image frames to

809   obtain the most reliable Pearson's correlation analysis (Fig. S3H).

810

811   <u>TICS and dual-color TICS</u>

812   Sample preparation and TIRF image series recording was performed as described for the Pearson's co-

813   localization analysis. In each pixel the time series are preprocessed to remove the frame-to-frame

814   variation of intensity using [41]:

$$I_{TICS}(x,y,t) = I(x,y,t) - \langle I(t) \rangle_{XY} + \langle I \rangle_{XY} \qquad \text{(Eq. 9)}$$

815   where $I(x,y,t)$ is the intensity of any pixel, $\langle I(t) \rangle_{XY}$ is the mean intensity of frame t and $\langle I \rangle_{XY}$ is the

816   mean intensity over all frames. The region inside the cell membrane was selected via freehand-

817   drawing. To exclude high-intensity clusters either dynamic (as described above for RICS) or static image

818   masking was applied (Videos S3-S5). For static region-of-interest (ROI) selection thresholding occurred

819   based on the average intensity of the whole time series. Pixel-based auto- and cross-correlations were

820   calculated using a one-dimensional discrete Fourier transform algorithm [40, 49]:

$$G(x,y,\tau) = \frac{\langle \delta I_{TICS,1}(x,y,t)\, \delta I_{TICS,2}(x,y,t+\tau) \rangle}{\langle I_{TICS,1}(x,y) \rangle \langle I_{TICS,2}(x,y) \rangle} \qquad \text{(Eq. 10)}$$

821   where τ is the time lag and $\delta I_{TICS,1} = \delta I_{TICS,2}$ for autocorrelation of a single imaging channel, while

822   for dual-color cross-correlation $\delta I_{TICS,1}$ and $\delta I_{TICS,2}$ are the values from the green and red image

823   respectively. Finally, a one-component model for 2D diffusion was fitted to the autocorrelation

824   functions (ACFs) and cross-correlation function (CCF) to obtain for each fit the average molecular

825   diffusion coefficient, D:

$$G_{TICS}(\tau) = A_D \left(1 + \frac{4D\tau}{\omega_r^2} \right)^{-1} + A_0 \qquad \text{(Eq. 11)}$$

826

827   where A_D is the amplitude of the decaying part of the correlation function, ω_r is the radial waist of

828   the point spread function (PSF) inherent to the resolution of the used microscope (Fig. S4A) and A_0 is

829   the offset caused by e.g. immobile molecules. To avoid influence of very slow motion (e.g. cell drift),

830   the data was fitted until a 12-frame lag (i.e., ~1 s). The relative cross-correlation was obtained by

831   dividing the amplitude of the cross-correlation function at the center by the mean of the two

832   amplitudes of the corresponding autocorrelation functions.

$$Rel.CC = \frac{G_{fit,CCF}(0)}{\left(G_{fit,ACF1}(0) + G_{fit,ACF2}(0) \right)/2} \qquad \text{(Eq. 12)}$$

833

Whole-cell patch-clamp electrophysiology

Cells were transfected with either GlyR-α3L-eGFP, GlyR-α3K-eGFP or GlyR-α3K-mCherry. Recordings were performed at room temperature in voltage-clamp mode using a HEKA EPC10 amplifier (HEKA Electronics, Lambrecht, Germany) controlled by HEKA acquisition software. Patch pipettes (3-4 MΩ) were filled with internal solution containing 120 mM CsCl , 2 mM Na_2ATP, 2 mM MgATP, 10 mM EGTA and 10 mM HEPES, adjusted to pH 7.2 with CsOH. The standard external solution (SES) had a composition of 150 mM NaCl, 5.4 mM KCl, 2 mM $CaCl_2$, 1 mM $MgCl_2$, 10 mM glucose and 10 mM HEPES. Glycinergic currents were recorded at a holding potential $V_H = -60\ mV$. Different glycine concentrations in SES including 20 μM, 50 μM, 100 μM, 200 μM, 500 μM were applied during 10 s. Maximum current amplitude was measured using FitMaster software (HEKA Electronics). The EC_{50} was calculated by plotting the normalized current as a function of concentration and fitting the data with the Hill equation (GraphPad Prism, La Jolla, CA, USA). For desensitization analysis, the decaying current phase was fitted using a mono-exponential in FitMaster software (HEKA Electronics, Lambrecht, Germany).

848

On-cell single-channel electrophysiology

Cells were transfected with either GlyR-α3L-eGFP, GlyR-α3K-mCherry or both GlyR-α3L-eGFP and GlyR-α3K-mCherry. On-cell recordings were performed in voltage clamp mode at RT using a HEKA EPC10 amplifier. The external solution contained 120 mM NaCl, 4.7 mM KCl, 2 mM CaCl2, 1.2 mM $MgCl_2$, 10 mM HEPES, 14 mM glucose, 20 mM TEA-Cl, 15 mM sucrose, adjusted to a pH of 7.4 with NaOH. Patch pipettes ($5-15$ MΩ) were filled with external solution and $30-80$ μM glycine. The holding potential was set at +60 mV. Analysis of on-cell recordings was done using the FitMaster software. Amplitude histograms from single-channel openings were made by manually selecting single-channel opening events with a constant baseline. Histograms were fit with a gaussian fit yielding a mean open amplitude for the event. A histogram was made from all amplitudes in which the most frequently occurring conductance states were identified and fit with a gaussian.

860

Summary of the Supplemental material

Fig. S1 shows the immunocytochemistry of the FP tagged GlyR. Fig. S2 illustrates the functional assessment of fluorescent protein tagged GlyR via electrophysiology, and shows the electrophysiology setup. Fig. S3 shows additional and control image correlation spectroscopy experiments. Fig. S4 shows focus size determination measurements of the Zeiss Elyra PS.1 and LSM880 microscopes. The supplementary tables include diffusion coefficients of the GlyR with frame-based thresholding (Table S1) and with average intensity-based thresholding (Table S2). Table S3 gives Pearson's correlation

868   coefficients to determine co-localization of GlyR-α3L and GlyR-α3K. Parameters obtaining from the

869   bleaching histograms fits are in Table S4. Brightness of eGFP tagged proteins can be found in Table S5.

References

1. Dutertre S, Becker C-M, Betz H. Inhibitory Glycine receptors: An update. The journal of biological Chemistry. 2012;287(48):40216-23.

2. Lynch JW, Zhang Y, Talwar S, Estrada-Mondragon A. Glycine Receptor Drug Discovery. Advances in Pharmacology. Elsevier; 2017. p. 225-53.

3. Nikolic Z, Laube B, Weber RG, Lichter P, Kioschis P, Poustka A, et al. The human glycine receptor subunit α3. Journal of Biological Chemistry. 1998;273(31):19708-14.

4. Uhlén M, Fagerberg L, Hallström BM, Lindskog C, Oksvold P, Mardinoglu A, et al. Tissue-based map of the human proteome. Science. 2015;347(6220).

5. Eichler S, Förstera B, Smolinsky B, Jüttner R, Lehmann T-N, Fähling M, et al. Splice-specific roles of glycine receptor a3 in the hippocampus. European Journal of Neuroscience. 2009;30:1077-91.

6. Winkelmann A, Maggio N, Eller J, Callskan G, Semtner M, Häussler U, et al. Changes in neural network homeostasis trigger neuropsychiatric symptoms. The Journal of Clinical investigation 2014;124:696-711.

7. Çalışkan G, Müller I, Semtner M, Winkelmann A, Raza AS, Hollnagel JO, et al. Identification of parvalbumin interneurons as cellular substrate of fear memory persistence. Cerebral Cortex. 2016;26(5):2325-40.

8. Eichler SA, Kirischuk S, Jüttner R, Schafermeier PK, Legendre P, Lehmann TN, et al. Glycinergic tonic inhibition of hippocampal neurons with depolarizing GABAergic transmission elicits histopathological signs of temporal lobe epilepsy. Journal of cellular and molecular medicine. 2008;12(6b):2848-66.

9. Harvey RJ, Depner UB, Wässle H, Ahmadi S, Heindl C, Reinold H, et al. GlyR α3: An Essential Target for Spinal PGE_2-Mediated Inflammatory Pain Sensitization. Science. 2004;304:884-7.

10. Malosio ML, Grenningloh G, Kuhse J, Schmieden V, Schmitt B, Prior P, et al. Alternative splicing generates two variants of the alpha 1 subunit of the inhibitory glycine receptor. Journal of Biological Chemistry. 1991;266(4):2048-53.

11. Kuhse J, Kuryatov A, Maulet Y, Malosio M, Schmieden V, Betz H. Alternative splicing generates two isoforms of the α2 subunit of the inhibitory glycine receptor. FEBS letters. 1991;283(1):73-7.

12. Oertel J, Villmann C, Kettenmann H, Kirchhoff F, Becker C-M. A Novel Glycine Receptor β Subunit Splice Variant Predicts an Unorthodox Transmembrane Topology ASSEMBLY INTO HETEROMERIC RECEPTOR COMPLEXES. Journal of Biological Chemistry. 2007;282(5):2798-807.

13. Zhang L-H, Gong N, Fei D, Xu L, Xu T-L. Glycine uptake regulates hippocampal network activity via glycine receptor-mediated tonic inhibition. Neuropsychopharmacology. 2008;33(3):701-11.

14. Meier JC, Semtner M, Winkelmann A, Wolfart J. Presynaptic mechanisms of neuronal plasticity and their role in epilepsy. Frontiers in cellular neuroscience. 2014;8:164.

15. Waseem TV, Fedorovich SV. Presynaptic glycine receptors influence plasma membrane potential and glutamate release. Neurochemical research. 2010;35(8):1188-95.

16. Kubota H, Alle H, Betz H, Geiger JR. Presynaptic glycine receptors on hippocampal mossy fibers. Biochemical and biophysical research communications. 2010;393(4):587-91.

17. Ruiz A, Campanac E, Scott RS, Rusakov DA, Kullmann DM. Presynaptic GABA A receptors enhance transmission and LTP induction at hippocampal mossy fiber synapses. Nature neuroscience. 2010;13(4):431.

18. Prior P, Schmitt B, Grenningloh G, Pribilla I, Multhaup G, Beyreuther K, et al. Primary structure and alternative splice variants of gephyrin, a putative glycine receptor-tubulin linker protein. Neuron. 1992;8(6):1161-70.

19. Meyer G, Kirsch J, Betz H, Langosch D. Identification of a gephyrin binding motif on the glycine receptor β subunit. Neuron. 1995;15(3):563-72.

20. Notelaers K, Smisdom N, Rocha S, Janssen D, Meier JC, Rigo J-M, et al. Ensemble and single particle fluorimetric techniques in concerted action to study the diffusion and aggregation of the glycine receptor α3 isoforms in the cell plasma membrane. biochimica et Biophysica Acta. 2012;1818:3131-40.

929 21. Notelaers K, Rocha S, Paesen R, Smisdom N, De Clercq B, Meier JC, et al. Analysis of α3 GlyR single
930 particle tracking in the cell membrane. Biochemica et Biophysica Acta. 2014;1843:544-53.

931 22. Notelaers K, Rocha S, Paesen R, Swinnen N, Vangindertael J, Meier JC, et al. Membrane distribution
932 of the glycine receptor α3 studied by optical super-resolution microscopy. Histochem Cell Biol.
933 2014;142:79-90.

934 23. Patrizio A, Renner M, Pizzarelli R, Triller A, Specht C. Alpha subunit-dependent glycine receptor
935 clustering and regulation of synaptic receptor numbers. Scientific reports. 2017;7(1):1-11.

936 24. Marabelli A, Moroni M, Lape R, Sivilotti LG. The kinetic properties of the α3 rat glycine receptor
937 make it suitable for mediating fast synaptic inhibition. The Journal of physiology. 2013;591(13):3289-
938 308.

939 25. Breitinger HG, Villmann C, Rennert J, Ballhausen D, Becker CM. Hydroxylated residues influence
940 desensitization behaviour of recombinant α3 glycine receptor channels. Journal of neurochemistry.
941 2002;83(1):30-6.

942 26. Acuña MA, Yévenes GE, Ralvenius WT, Benke D, Di Lio A, Lara CO, et al. Phosphorylation state-
943 dependent modulation of spinal glycine receptors alleviates inflammatory pain The Journal of Clinical
944 investigation. 2016;126(7):2547-60.

945 27. Lara CO, Murath P, Muñoz B, Marileo AM, San Martín L, San Martín VP, et al. Functional modulation
946 of glycine receptors by the alkaloid gelsemine. British journal of pharmacology. 2016;173(14):2263-77.

947 28. Moraga-Cid G, San Martín VP, Lara CO, Muñoz B, Marileo AM, Sazo A, et al. Modulation of glycine
948 receptor single-channel conductance by intracellular phosphorylation. Scientific reports. 2020;10(1):1-
949 11.

950 29. Bormann J, Rundström N, Betz H, Langosch D. Residues within transmembrane segment M2
951 determine chloride conductance of glycine receptor homo-and hetero-oligomers. The EMBO Journal.
952 1993;12(10):3729-37.

953 30. Schwille P, Meyer-Almes F-J, Rigler R. Dual-color fluorescence cross-correlation spectroscopy for
954 multicomponent diffusional analysis in solution. Biophys J. 1997;72(4):1878-86.

955 31. Digman MA, Wiseman PW, Horwitz AR, Gratton E. Detecting protein complexes in living cells from
956 laser scanning confocal image sequences by the cross correlation raster image spectroscopy method.
957 Biophys J. 2009;96(2):707-16.

958 32. McGuire H, Aurousseau MR, Bowie D, Blunck R. Automating single subunit counting of membrane
959 proteins in mammalian cells. Journal of Biological Chemistry. 2012;287(43):35912-21.

960 33. Ulbrich MH, Isacoff EY. Subunit counting in membrane-bound proteins. Nature methods.
961 2007;4(4):319-21.

962 34. Watanabe N, Mitchison TJ. Single-molecule speckle analysis of actin filament turnover in
963 lamellipodia. Science. 2002;295(5557):1083-6.

964 35. Groot-Kormelink PJ, Beato M, Finotti C, Harvey RJ, Sivilotti LG. Achieving optimal expression for
965 single channel recording: a plasmid ratio approach to the expression of α1 glycine receptors in HEK293
966 cells. Journal of neuroscience methods. 2002;113(2):207-14.

967 36. Wong K, Briddon SJ, Holliday ND, Kerr ID. Plasma membrane dynamics and tetrameric organisation
968 of ABCG2 transporters in mammalian cells revealed by single particle imaging techniques. Biochimica
969 et Biophysica Acta (BBA)-Molecular Cell Research. 2016;1863(1):19-29.

970 37. Brown C, Dalal R, Hebert B, Digman M, Horwitz A, Gratton E. Raster image correlation spectroscopy
971 (RICS) for measuring fast protein dynamics and concentrations with a commercial laser scanning
972 confocal microscope. Journal of microscopy. 2008;229(1):78-91.

973 38. Digman MA, Brown CM, Sengupta P, Wiseman PW, Horwitz AR, Gratton E. Measuring fast dynamics
974 in solutions and cells with a laser scanning microscope. Biophys J. 2005;89(2):1317-27.

975 39. Digman MA, Sengupta P, Wiseman PW, Brown CM, Horwitz AR, Gratton E. Fluctuation correlation
976 spectroscopy with a laser-scanning microscope: exploiting the hidden time structure. Biophys J.
977 2005;88(5):L33-L6.

978 40. Wiseman P, Squier J, Ellisman M, Wilson K. Two-photon image correlation spectroscopy and image
979 cross-correlation spectroscopy. Journal of microscopy. 2000;200(1):14-25.

41. Hendrix J, Baungärtel V, Schrimpf W, Ivanchenko S, Digman MA, Gratton E, et al. Live-cell observation of cytosolic HIV-1 assembly onset reveals RNA-interacting Gag oligomers. J Cell Biol. 2015;210(4):629-49.

42. Longfils M, Smisdom N, Ameloot M, Rudemo M, Lemmens V, Fernández GS, et al. Raster Image Correlation Spectroscopy Performance Evaluation. Biophysical journal. 2019;117(10):1900-14.

43. Kolin DL, Costantino S, Wiseman PW. Sampling effects, noise, and photobleaching in temporal image correlation spectroscopy. Biophysical journal. 2006;90(2):628-39.

44. Manders E, Stap J, Brakenhoff G, Van Driel R, Aten J. Dynamics of three-dimensional replication patterns during the S-phase, analysed by double labelling of DNA and confocal microscopy. Journal of cell science. 1992;103(3):857-62.

45. Bolte S, Cordelières FP. A guided tour into subcellular colocalization analysis in light microscopy. Journal of microscopy. 2006;224(3):213-32.

46. Dunn KW, Kamocka MM, McDonald JH. A practical guide to evaluating colocalization in biological microscopy. American Journal of Physiology-Cell Physiology. 2011;300(4):C723-C42.

47. Hendrix J, Gijsbers R, De Rijck J, Voet A, Hotta J-i, McNeely M, et al. The transcriptional co-activator LEDGF/p75 displays a dynamic scan-and-lock mechanism for chromatin tethering. Nucleic acids research. 2011;39(4):1310-25.

48. Schrimpf W, Lemmens V, Smisdom N, Ameloot M, Lamb DC, Hendrix J. Crosstalk-free multicolor RICS using spectral weighting. Methods. 2018;140:97-111.

49. Srivastava M, Petersen NO. Diffusion of transferrin receptor clusters. Biophys Chem. 1998;75(3):201-11.

50. Hendrix J, Dekens T, Schrimpf W, Lamb DC. Arbitrary-Region Raster Image Correlation Spectroscopy. Biophys J. 2016;111:1-12.

51. Fogarty KH, Chen Y, Grigsby IF, Macdonald PJ, Smith EM, Johnson JL, et al. Characterization of cytoplasmic Gag-gag interactions by dual-color z-scan fluorescence fluctuation spectroscopy. Biophysical journal. 2011;100(6):1587-95.

52. Vercammen J, Maertens G, Gerard M, De Clercq E, Debyser Z, Engelborghs Y. DNA-induced polymerization of HIV-1 integrase analyzed with fluorescence fluctuation spectroscopy. Journal of Biological Chemistry. 2002;277(41):38045-52.

53. Lemmens V, Ramanathan K, Hendrix J. Fluorescence microscopy data for quantitative mobility and interaction analysis of proteins in living cells. Data in brief. 2020:105348.

54. Gambin Y, Lopez-Esparza R, Reffay M, Sierecki E, Gov N, Genest M, et al. Lateral mobility of proteins in liquid membranes revisited. Proceedings of the National Academy of Sciences. 2006;103(7):2098-102.

55. Naji A, Levine AJ, Pincus PA. Corrections to the Saffman-Delbrück mobility for membrane bound proteins. Biophysical journal. 2007;93(11):L49-L51.

56. Choquet D. Fast AMPAR trafficking for a high-frequency synaptic transmission. European Journal of Neuroscience. 2010;32(2):250-60.

57. Weltzien F, Puller C, O'Sullivan GA, Paarmann I, Betz H. Distribution of the glycine receptor β-subunit in the mouse CNS as revealed by a novel monoclonal antibody. Journal of Comparative Neurology. 2012;520(17):3962-81.

58. Meier J, Grantyn R. A gephyrin-related mechanism restraining glycine receptor anchoring at GABAergic synapses. Journal of Neuroscience. 2004;24(6):1398-405.

59. Durisic N, Godin AG, Wever CM, Heyes CD, Lakadamyali M, Dent JA. Stoichiometry of the Human Glycine receptor revealed by direct subunit counting. The Journal of Neuroscience. 2012;32:12915-20.

60. Schaefer N, Roemer V, Janzen D, Villmann C. Impaired Glycine receptor trafficking in neurological diseases. Frontiers in Molecular Neuroscience. 2018;11:291.

61. van Steensel B, van Binnendijk EP, Hornsby CD, Van der Voort H, Krozowski ZS, de Kloet ER, et al. Partial colocalization of glucocorticoid and mineralocorticoid receptors in discrete compartments in nuclei of rat hippocampus neurons. Journal of cell science. 1996;109(4):787-92.

62. Förstera B, a Dzaye OD, Winkelmann A, Semtner M, Benedetti B, Markovic DS, et al. Intracellular glycine receptor function facilitates glioma formation in vivo. Journal of Cell Science. 2014;127(17):3687-98.

63. Kluba M, Engelborghs Y, Hofkens J, Mizuno H. Inhibition of receptor dimerization as a novel negative feedback mechanism of EGFR signaling. PLoS One. 2015;10(10):e0139971.

64. Pack C, Saito K, Tamura M, Kinjo M. Microenvironment and effect of energy depletion in the nucleus analyzed by mobility of multiple oligomeric EGFPs. Biophysical journal. 2006;91(10):3921-36.

65. Chen C, Okayama H. High-efficiency transformation of mammalian cells by plasmid DNA. Molecular and cellular biology. 1987;7(8):2745-52.

66. Liebsch F, Aurousseau MR, Bethge T, McGuire H, Scolari S, Herrmann A, et al. Full-length cellular β-secretase has a trimeric subunit stoichiometry, and its sulfur-rich transmembrane interaction site modulates cytosolic copper compartmentalization. Journal of Biological Chemistry. 2017;292(32):13258-70.

67. Dunsing V, Luckner M, Zühlke B, Petazzi RA, Herrmann A, Chiantia S. Optimal fluorescent protein tags for quantifying protein oligomerization in living cells. Scientific reports. 2018;8(1):1-12.

68. Godin AG, Rappaz B, Potvin-Trottier L, Kennedy TE, De Koninck Y, Wiseman PW. Spatial intensity distribution analysis reveals abnormal oligomerization of proteins in single cells. Biophysical journal. 2015;109(4):710-21.

69. Arant RJ, Ulbrich MH. Deciphering the subunit composition of multimeric proteins by counting photobleaching steps. ChemPhysChem. 2014;15(4):600-5.

70. Hines KE. Inferring subunit stoichiometry from single molecule photobleaching. Journal of General Physiology. 2013;141(6):737-46.

71. Schrimpf W, Barth A, Hendrix J, Lamb DC. PAM: A framework for integrated analysis of imaging, single-molecule, and ensemble fluorescence data. Biophysical journal. 2018;114(7):1518-28.

72. METS RD, Delon A, Balland M, Destaing O, Wang I. Dynamic range and background filtering in raster image correlation spectroscopy. Journal of Microscopy. 2020.

73. Ivanchenko S, Lamb DC. Fluorescence correlation spectroscopy: principles and developments. Supramolecular Structure and Function 10. Springer, Dordrecht; 2011. p. 1-30.